



Chemical Diversity on Small Scales: Abundance Analysis of the Tucana V Ultrafaint Dwarf Galaxy

Terese T. Hansen¹ , Joshua D. Simon² , Ting S. Li³ , Domani Sharkey⁴, Alexander P. Ji⁵ , Ian B. Thompson², Henrique M. Reggiani^{2,6} , and Jhon Yana Galarza²

¹ Department of Astronomy, Stockholm University, AlbaNova University Center, SE-106 91 Stockholm, Sweden; thidemannhansen@gmail.com

² Observatories of the Carnegie Institution for Science, 813 Santa Barbara St., Pasadena, CA 91101, USA

³ Department of Astronomy and Astrophysics, University of Toronto, 50 St. George St., Toronto, ON M5S 3H4, Canada

⁴ Department of Astronomy, California Institute of Technology, 1200 E. California Blvd., Pasadena, CA 91125, USA

⁵ Department of Astronomy & Astrophysics, University of Chicago, 5640 S. Ellis Ave., Chicago, IL 60637, USA

⁶ Gemini Observatory/NSF's NOIRLab, Casilla 603, La Serena, Chile

Received 2023 December 1; revised 2024 March 18; accepted 2024 March 18; published 2024 June 5

Abstract

The growing number of Milky Way satellites detected in recent years has introduced a new focus for stellar abundance analysis. Abundances of stars in satellites have been used to probe the nature of these systems and their chemical evolution. However, for most satellites, only centrally located stars have been examined. This paper presents an analysis of three stars in the Tucana V system, one in the inner region and two at $\sim 10'$ (7–10 half-light radii) from the center. We find a remarkable chemical diversity between the stars. One star exhibits enhancements in rapid neutron-capture elements (an *r*-I star), and another is highly enhanced in C, N, and O but with low neutron-capture abundances (a CEMP-no star). The metallicities of the stars analyzed span more than 1 dex from $[\text{Fe}/\text{H}] = -3.55$ to -2.46 . This, combined with a large abundance range of other elements like Ca, Sc, and Ni, confirms that Tuc V is an ultrafaint dwarf (UFD) galaxy. The variation in abundances, highlighted by $[\text{Mg}/\text{Ca}]$ ratios ranging from $+0.89$ to -0.75 , among the stars demonstrates that the chemical enrichment history of Tuc V was very inhomogeneous. Tuc V is only the second UFD galaxy in which stars located at large distances from the galactic center have been analyzed, along with Tucana II. The chemical diversity seen in these two galaxies, driven by the composition of the noncentral member stars, suggests that distant member stars are important to include when classifying faint satellites and that these systems may have experienced more complex chemical enrichment histories than previously anticipated.

Unified Astronomy Thesaurus concepts: Stellar abundances (1577); Dwarf galaxies (416); Milky Way stellar halo (1060)

Supporting material: machine-readable tables

1. Introduction

The population of Milky Way (MW) satellites has exploded over the last decade, especially at the faint end. Currently, 44 satellites that have luminosities $L \leq 1000 L_\odot$ ($M_V \geq -2.7$) have been discovered, only eight of which were known prior to 2013. These stellar systems range in half-light radius from 1 to 90 pc and in distance from 5 to 250 kpc and have luminosities as faint as $45 L_\odot$.

Determining the nature of such diminutive objects has proven to be a major challenge. Are they dark-matter-dominated dwarf galaxies or dark-matter-free star clusters? Did they reach their tiny sizes and luminosities via tidal stripping of larger systems, or did they form close to their current size? Published spectroscopy to provide dynamical masses and chemical abundance information is available for only a small minority of this population. Consequently, in most cases, they have been classified based solely on their physical size, with satellites at $r_{\text{half}} \lesssim 10$ pc regarded as clusters, those with $r_{\text{half}} \gtrsim 30$ pc regarded as dwarfs, and the nature of those in between remaining uncertain. In a few cases, the stellar kinematics and/or chemistry (Geha et al. 2009; Fadely et al.

2011; Simon et al. 2011; Kirby et al. 2013a; Ji et al. 2019b, 2020b; Fu et al. 2023) have provided relatively confident classifications. Most recently, measurements of mass segregation from deep imaging have provided a promising route for separating dynamically relaxed clusters from dwarf galaxies that have not relaxed because of their large dark matter content (Kim et al. 2015; Baumgardt et al. 2022).

A representative object in this category is Tucana V (Tuc V), which was discovered in imaging from the Dark Energy Survey (DES) by Drlica-Wagner et al. (2015). Tuc V has a luminosity of $240^{+170}_{-90} L_\odot$ and a half-light radius of 34^{+11}_{-8} pc (somewhat larger than the initially estimated 17 ± 6 pc from Drlica-Wagner et al. 2015) and is located at a distance of 55^{+3}_{-8} kpc (Simon et al. 2020). Based on its diffuse appearance in deep imaging, Conn et al. (2018) suggested that Tuc V is either an unbound part of the halo of the Small Magellanic Cloud (SMC) or a tidally disrupted star cluster. On the other hand, Simon et al. (2020) obtained medium-resolution spectroscopy of Tuc V, identifying three stars as spectroscopic members of the system and showing that their velocities and proper motions are not consistent with those of the SMC. Given this very small set of faint member stars, Simon et al. were not able to place meaningful constraints on the velocity dispersion or metallicity dispersion of Tuc V. However, Fu et al. (2023) tentatively detected a metallicity spread in Tuc V of $\sigma_{[\text{Fe}/\text{H}]} = 0.61^{+0.44}_{-0.28}$ dex using Hubble Space Telescope narrowband imaging.



Original content from this work may be used under the terms of the [Creative Commons Attribution 4.0 licence](https://creativecommons.org/licenses/by/4.0/). Any further distribution of this work must maintain attribution to the author(s) and the title of the work, journal citation and DOI.

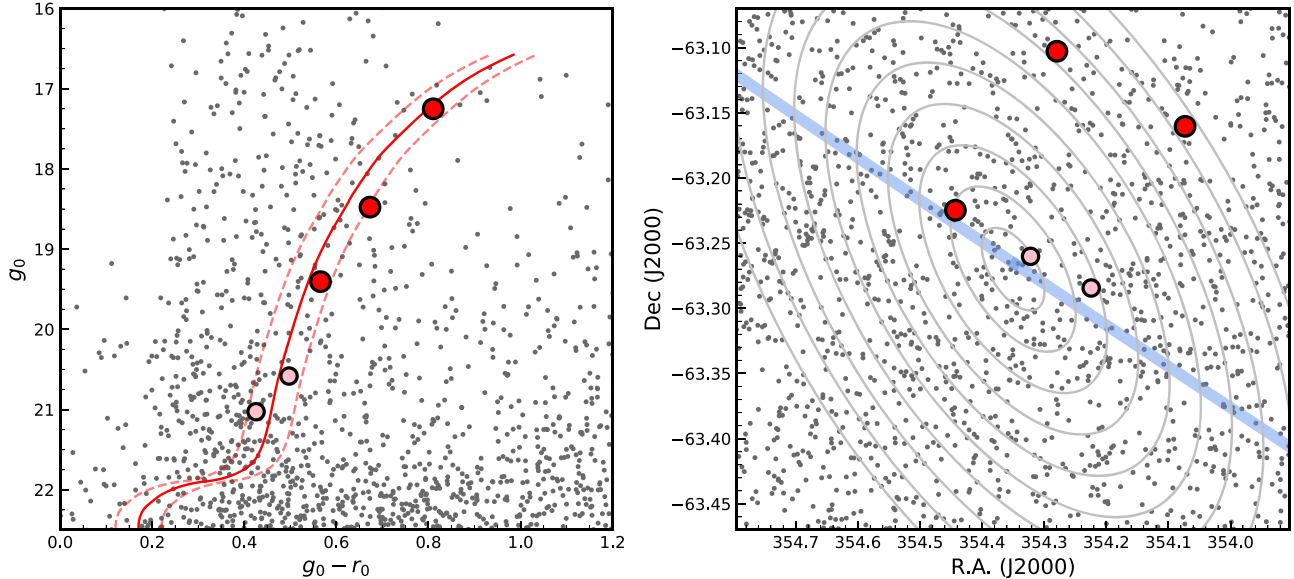


Figure 1. (Left) Color-magnitude diagram of a $24' \times 24'$ field centered on Tuc V, using photometry from DES DR1 (Abbott et al. 2018). The three stars that are the subject of this paper are plotted as red circles, and the two fainter members of Tuc V from Simon et al. (2020) are shown as smaller pink circles. A 12 Gyr, $[\text{Fe}/\text{H}] = -2.49$ Dartmouth isochrone (Dotter et al. 2008) at a distance of 55 kpc is displayed in red, with additional curves (dashed lines) offset by ± 0.05 mag illustrating a typical photometric selection window around the isochrone. (Right) Spatial distribution of stars around Tuc V. The symbols are the same as in the left panel. Ellipses marking 1, 2, ..., 10 times the half-light radius of Tuc V are displayed in gray. The orbital path of Tuc V, computed with galpy (Bovy 2015) based on the proper motion from Pace et al. (2022) and the updated radial velocity determined in Section 5.1, is plotted as a thick blue line.

In this paper, we present a detailed chemical analysis of three stars in Tuc V: one located in the center of the system, Gaia DR3 6486878326228216320 (hereafter Tuc V-3), included in the sample of Simon et al. (2020), and two newly detected members located at larger radii, Gaia DR3 6486893242650962944 and Gaia DR3 6486519060804598016 (hereafter Tuc V-1 and Tuc V-2, respectively). We further use this information to constrain the nature of Tuc V and investigate the chemical enrichment of the system. The paper is organized as follows: observations and analyses of the stars are described in Sections 2 and 3; Section 4 presents our results, which are discussed in Section 5; and Section 6 provides a summary.

2. Observations

2.1. Target Selection

The three Tuc V member stars identified by Simon et al. (2020) have magnitudes of $g = 19.42$, $g = 20.60$, and $g = 21.06$. The brightest of these (Tuc V-3) is accessible for high-resolution spectroscopy with long exposure times (see Simon et al. 2010; Frebel et al. 2014), but the other two stars are too faint for chemical abundance analysis from high-resolution spectra with current instruments. However, we used astrometry from Gaia Early Data Release 3 (Gaia Collaboration et al. 2016, 2021) to identify two substantially brighter stars with proper motions matching that of the brightest Simon et al. member (Tuc V-1 and Tuc V-2). These stars, at $G = 16.57$ and $G = 17.92$, are both located $\sim 10'$ ($\sim 5r_{\text{half}}$, although their projected distances are larger because they are located close to the minor axis) from the center of Tuc V and have colors and magnitudes that are consistent with the Tuc V red giant branch (see Figure 1). Although it would be surprising for the two brightest stars in the system to be located at such large radii if Tuc V has an extended envelope similar to ultrafaint dwarf (UFD) galaxies such as Tucana II (Chiti et al. 2021) or Boötes I (Filion & Wyse 2021; Longeard et al. 2022), these stars could

plausibly be Tuc V members. In order to test this possibility, we obtained high-resolution spectroscopy of the brightest confirmed Tuc V member, as well as the two new candidates.

2.2. Magellan/MIKE Spectroscopy

The high-resolution spectra of the three stars used for abundance analysis were obtained with the MIKE spectrograph (Bernstein et al. 2003; Shectman & Johns 2003) on the Magellan/Clay Telescope at Las Campanas Observatory in 2021 August, 2021 December, and 2022 August. Additional low signal-to-noise ratio (S/N) MIKE spectra of Tuc V-1 for radial velocity measurements were also obtained through 2023 August. Table 1 lists target Gaia DR3 IDs, R.A., decl., DES DR1 magnitudes, the Modified Julian Date (MJD) of the observations, exposure times, S/N, and heliocentric velocities for the spectra. The radial velocities are determined via χ^2 fits of the spectra with a template spectrum of the radial velocity standard star HD 122563 ($V_{\text{hel}} = -26.17 \text{ km s}^{-1}$; Gaia Collaboration et al. 2021) also obtained with the MIKE spectrograph, as described by Ji et al. (2020b). The MIKE spectra cover wavelength ranges of $3330 \text{ \AA} < \lambda < 5060 \text{ \AA}$ in the blue channel and $4830 \text{ \AA} < \lambda < 9410 \text{ \AA}$ in the red. For Tuc V-3, the $1'' \times 5''$ slit and 2×2 binning were used, yielding a typical resolution of $R \sim 28,000/22,000$ in the blue and red arms, and for the other two stars, the $0''.7 \times 5''$ slit and 2×2 binning were used, yielding a typical resolution of $R \sim 35,000/28,000$ in the blue and red arms. All data were reduced with the CarPy MIKE pipeline (Kelson et al. 2000; Kelson 2003), and multiple spectra of the same star from different runs were subsequently coadded. The seeing on the observing nights listed in Table 1 varied from $0''.5$ to $1''.4$, but for most of the observations, the seeing was not significantly smaller than the slit width. Thus, slit centering has not resulted in any meaningful offsets on the measured radial velocities as confirmed by the good agreement between individual measurements of Tuc V-2 and Tuc V-3.

Table 1
Observing Log

Gaia DR3 ID	R.A.	Decl.	g_0 (mag)	r_0 (mag)	i_0 (mag)	z_0 (mag)	MJD	t_{exp} (s)	S/N* @4500 Å	S/N* @6500 Å	$V_{\text{hel}} \pm \sigma$ (km s $^{-1}$)	Instrument
6486893242650962944 (Tuc V-1)	23:37:07.09	−63:06:10.2	17.25	16.44	16.13	15.99	59437.15	10,800	22	51	−23.9 ± 0.6	MIKE
...	59552.03	900	−42.0 ± 1.2	MIKE
...	59812.31	300	−23.8 ± 1.6	MIKE
...	59881.02	360	−37.4 ± 1.2	IMACS
...	60095.41	900	−26.1 ± 1.0	MIKE
...	60106.39	780	−26.3 ± 1.1	IMACS
...	60113.27	1200	−24.0 ± 1.4	MIKE
...	60177.43	2200	−21.2 ± 1.4	MIKE
...	60250.02	600	−33.7 ± 1.7	IMACS
...	60281.06	960	−37.7 ± 1.1	MIKE
...	60306.06	960	−41.8 ± 1.3	MIKE
6486519060804598016 (Tuc V-2)	23:36:17.58	−63:09:37.6	18.48	17.80	17.56	17.43	59437.23	19,900	19	44	−33.8 ± 0.6	MIKE
...	59813.13	11,700	−34.5 ± 0.6	MIKE
6486878326228216320 (Tuc V-3)	23:37:46.33	−63:13:29.2	19.41	18.84	18.63	18.54	59437.39	9900	15	33	−35.4 ± 1.6	MIKE
...	59551.17	10,800	−36.1 ± 0.9	MIKE
...	59552.14	8400	−36.4 ± 1.7	MIKE
...	59813.31	18,120	−36.0 ± 0.9	MIKE

Note. An asterisk indicates S/N is measured in coadded MIKE spectra used for abundance analysis.

2.3. Magellan/IMACS Spectroscopy

We obtained two additional spectra of Tuc V-1 in 2022 October and 2023 June with the IMACS spectrograph (Dressler et al. 2011) on the Magellan/Baade telescope to measure its radial velocity. For these observations, we employed a $0''.7$ wide long slit with the 1200 line grating on the $f/4$ camera, resulting in a resolution of $R \sim 11,000$. Data reduction and analysis procedures followed those described by Li et al. (2017) and Simon et al. (2017) and subsequent papers.

2.4. Tuc V Membership

Using the initial MIKE spectrum of Tuc V-2, we measured a velocity of $v_{\text{hel}} = -33.8 \pm 0.6 \text{ km s}^{-1}$ and a metallicity of $[\text{Fe}/\text{H}] < -2$. This velocity agrees within the uncertainties with the systemic velocity of Tuc V ($-36.2^{+2.5}_{-2.2} \text{ km s}^{-1}$; Simon et al. 2020) and, combined with the low metallicity, confirms that the star belongs to Tuc V. In contrast, our first velocity measurement for Tuc V-1 was offset from Tuc V by 12 km s^{-1} . However, the extremely low metallicity of this star makes it very unlikely to be a foreground halo star unrelated to Tuc V. We therefore suspected that the star is a member of Tuc V with a binary companion and began monitoring its radial velocity. The subsequent measurements listed in Table 1 confirmed this hypothesis, revealing periodic orbital motion with a center-of-mass velocity close to that of the other Tuc V stars. It is thus safe to conclude that both bright stars are Tuc V members. Velocity measurements of Tuc V-2 and Tuc V-3 spanning 1 yr for each star show no evidence of velocity variability, indicating that neither star is likely to be in a binary system with a period shorter than several years.

As mentioned above, these two new Tuc V stars are located at large distances from the center of the system. If Tuc V has a normal exponential or Plummer radial profile, it is very unlikely that two of its handful of red giants would be found at $\gtrsim 7r_{\text{half}}$. This result, therefore, suggests that either the size of Tuc V has been significantly underestimated or it has an extended stellar component with a different radial profile. In the latter case, the Tuc V halo could have originated in an ancient merger (e.g., Chiti et al. 2021; Tarumi et al. 2021; Goater et al. 2024) or could indicate that Tuc V is undergoing tidal stripping by the MW. We encourage deeper and wider imaging of Tuc V to explore these possibilities further.

3. Abundance Analysis

The spectral analysis was done using the analysis code SMHR⁷ to run the 2017 version of the radiative transfer code MOOG⁸ (Sneden 1973; Sobeck et al. 2011). The analysis assumes that local thermodynamical equilibrium and one-dimensional α -enhanced ($[\alpha/\text{Fe}] = +0.4$) ATLAS9 model atmospheres (Castelli & Kurucz 2003) were used as input. The line lists used were generated from linemake⁹ (Placco et al. 2021) and include isotopic (IS) and hyperfine structure (HFS) broadening, where applicable, employing the r -process isotope ratios from Sneden et al. (2008). Finally, solar abundances were taken from Asplund et al. (2009).

The stellar parameters were determined from a combination of photometry and equivalent width (EW) measurements of

Table 2
Stellar Parameters

ID	T_{eff} (K)	$\log g$ (cgs)	ξ (km s^{-1})	$[\text{Fe}/\text{H}]$
Tuc V-1	4380 ± 104	0.54 ± 0.32	2.18 ± 0.09	-3.47 ± 0.21
Tuc V-2	4773 ± 92	1.53 ± 0.21	1.91 ± 0.08	-2.41 ± 0.15
Tuc V-3	4982 ± 130	1.70 ± 0.20	1.61 ± 0.13	-2.57 ± 0.25

Fe I and Fe II lines obtained by fitting Gaussian profiles to the absorption lines in the continuum-normalized spectra. Photometric effective temperatures (T_{eff}) were determined from dereddened g , r , i , and z colors from DES DR1 (Abbott et al. 2018), listed in Table 1, converted to the corresponding B , V , R , and I colors¹⁰ (Drlica-Wagner et al. 2018) and employing the $B - V$, $V - R$, $R - I$, and $V - I$ color temperature relations from Casagrande et al. (2010). The final temperature is taken as an average of the four indicators. Individual temperatures from the four colors are listed in Table A1, along with spectroscopic temperatures for the stars that have been placed on a photometric scale using the relation from Frebel et al. (2013). The photometric and corrected spectroscopic temperatures agree within the uncertainties. In the top panel of Figure A1, we plot the Fe I and Fe II line abundances as a function of excitation potential (χ). A small trend is visible in these plots due to the offset between the spectroscopic and photometric temperature scales. Following the determination of T_{eff} , the surface gravities ($\log g$) were determined from ionization equilibrium between the Fe I and Fe II lines and microturbulent velocities (ξ) by removing any trend in line abundances with reduced EW for the Fe I lines (see Figure A1). The model atmosphere metallicity ($[\text{M}/\text{H}]$) is taken as the mean of the Fe I and Fe II abundances. Final stellar parameters and their uncertainties are presented in Table 2. The uncertainty on T_{eff} is taken as the standard deviation of T_{eff} from the four colors used and the effect of the standard deviation of the abundances of the Fe I lines used added in quadrature. Uncertainties on $\log g$, $[\text{M}/\text{H}]$, and ξ are the result of the photometric uncertainty on T_{eff} and the standard deviation of the abundances of the Fe I lines used added in quadrature. The effects of the standard deviation of the Fe I line abundances were determined by varying each parameter (T_{eff} , $\log g$, and ξ) one at a time to match the standard deviation of Fe I line abundances. Individual stellar parameter uncertainties are listed in Table A2.

Following the stellar parameter determination, elemental abundances were derived from EW measurements and spectral synthesis. Table 3 lists the atomic data for the lines used in the analysis and the measured EW and abundance of each line. Final mean abundances and associated uncertainties were determined following the procedure outlined in Ji et al. (2020a). This method performs a line-by-line analysis and includes both statistical and systematic uncertainties and covariance terms between stellar parameter uncertainties.

4. Abundance Results

Our final abundances and total associated uncertainties for the three stars are listed in Table 4. Abundance uncertainties arising from individual stellar parameters (Δ_X) are listed in

⁷ <https://github.com/andycasey/smhr>

⁸ <https://github.com/alexji/moog17scat>

⁹ <https://github.com/vmplacco/linemake>

¹⁰ Lupton (2005) <http://www.sdss3.org/dr8/algorithms/sdssUBVRITransform.php>.

Table 3
Data for Atomic Lines Used in Analysis and Individual Line EW Measurements for Each Star

ID	Species	λ (Å)	χ (eV)	$\log gf$	EW (mA)	σ_{EW} (mA)	$\log \epsilon$	References
Tuc V-1	8.0	6300.30	0.00	-9.69	31.01	4.67	+6.92	(1)
Tuc V-1	8.0	7771.94	9.15	+0.37	11.01	4.47	+7.46	(1)
Tuc V-1	8.0	7775.39	9.15	0.00	14.01	3.10	+7.97	(1)
Tuc V-1	11.0	5889.95	0.00	+0.11	206.25	3.80	+3.94	(1)
Tuc V-1	11.0	5895.92	0.00	-0.19	180.34	3.60	+3.90	(1)
Tuc V-1	11.0	8183.26	2.10	+0.24	25.62	2.91	+3.49	(1)
Tuc V-1	11.0	8194.81	2.10	+0.49	48.89	3.22	+3.64	(1)
Tuc V-1	12.0	4057.51	4.35	-0.90	63.95	6.38	+5.52	(1)

Note. Atomic numbers are listed under species.

References. (1) Kramida et al. (2023); (2) Pehlivan Rhodin et al. (2017); (3) Den Hartog et al. (2023); (4) Den Hartog et al. (2021); (5) Lawler et al. (2019); (6) Lawler et al. (2013); (7) Wood et al. (2013); (8) Pickering et al. (2001), with corrections given in Pickering et al. (2002); (9) Wood et al. (2014a) for $\log(gf)$ values and HFS, when available; (10) Sobeck et al. (2007); (11) Lawler et al. (2017); (12) Den Hartog et al. (2011) for both $\log(gf)$ value and HFS; (13) O'Brian et al. (1991); (14) Ruffoni et al. (2014); (15) Belmonte et al. (2017); (16) Den Hartog et al. (2014); (17) Blackwell et al. (1982); (18) Den Hartog et al. (2019); (19) Meléndez & Barbuy (2009); (20) Lawler et al. (2015) for $\log(gf)$ values and HFS; (21) Wood et al. (2014b); (22) Roederer & Lawler (2012); (23) Biémont et al. (2011); (24) Ljung et al. (2006); (25) Kramida et al. (2023), using HFS/IS from McWilliam (1998) when available; (26) Lawler et al. (2001a), using HFS from Ivans et al. (2006) when available; (27) Lawler et al. (2009); (28) Li et al. (2007), using HFS from Sneden et al. (2009); (29) Ivarsson et al. (2001), using HFS from Sneden et al. (2009); (30) Lawler et al. (2001b), using HFS/IS from Ivans et al. (2006); (31) Wickliffe et al. (2000).

(This table is available in its entirety in machine-readable form.)

Table 5 along with the systematic uncertainty s_x . We were able to derive abundances for 15 elements from C to Ba in all three stars and additional elements in Tuc V-2 and Tuc V-1 (see details below). Abundances of elements from C to Eu of the three stars are shown in Figure 2 compared to abundance results from high-resolution ($R \gtrsim 25,000$) studies of other UFD galaxies and metal-poor MW halo stars (Roederer et al. 2014). Only abundance detections have been included in the comparison sample. The UFD galaxies with literature abundance measurements are Boötes I (Feltzing et al. 2009; Norris et al. 2010; Gilmore et al. 2013; Ishigaki et al. 2014; Frebel et al. 2016; Waller et al. 2023), Boötes II (Ji et al. 2016b), Carina II (Ji et al. 2020b), Carina III (Ji et al. 2020b), Cetus II (Webber et al. 2023), Coma Berenices (Frebel et al. 2010; Waller et al. 2023), Grus I (Ji et al. 2019b), Grus II (Hansen et al. 2020), Hercules (Koch et al. 2008), Horologium I (Nagasawa et al. 2018), Leo IV (Simon et al. 2010), Pisces II (Spite et al. 2018), Reticulum II (Ji et al. 2016a, 2016c; Hayes et al. 2023), Segue 1 (Norris et al. 2010; Frebel et al. 2014), Segue 2 (Roederer & Kirby 2014), Triangulum II (Ji et al. 2019b), Tucana II (Ji et al. 2016d; Chiti et al. 2018, 2023), Tucana III (Hansen et al. 2017; Marshall et al. 2019), Ursa Major I (Waller et al. 2023), and Ursa Major II (Frebel et al. 2010).

4.1. CNO and Odd Z Elements

Carbon abundances were derived via spectral synthesis of the C–H G band at 4313 Å, as shown in Figure 3. As no O abundance could be derived for Tuc V-3 and Tuc V-2, we assumed a standard oxygen enhancement for metal-poor stars of $[\text{O}/\text{Fe}] = 0.4$ when deriving the C abundances from these two stars. We have corrected the C abundances of all three stars for the effects of stellar evolution following Placco et al. (2014). These values are listed in Table 4 under C_{corr} . One of the stars, Tuc V-1, qualifies as a carbon-enhanced metal-poor (CEMP; Beers & Christlieb 2005) star, with $[\text{C}/\text{Fe}] > 0.7$ (Aoki et al. 2007). For this star, we also derive an O abundance from the 6300, 7772, and 7775 Å lines and an N abundance

from the CN band at 3880 Å. The star is enhanced in both O and N, as has also been seen for MW halo CEMP stars (Norris et al. 2013). Na abundances are derived from EW measurements of the 5688, 5889, 5895, 8183, and 8194 Å lines and Al abundances from synthesis of the 3944 and 3961 Å lines. Figure 4 shows the fit of the 5895 Å Na I line in the three stars. The CEMP star, Tuc V-1, has a very high $[\text{Na}/\text{Fe}]$ ratio, a signature that, to some extent, is also present in Tuc V-2, while Tuc V-3 is more similar to the literature values for UFD galaxy stars (see Figure 2). K abundances are derived from EW measurements of the 7664 and 7698 Å lines and Sc abundances from a synthesis of 10 lines (see Table 3 for details). All three stars have high K abundances ($[\text{K}/\text{Fe}] > 0.5$), a unique signature found only in some UFD galaxies (Webber et al. 2023).

4.2. α and Iron-peak Elements

Abundances for Mg, Si, Ca, Ti, Cr, and Ni are derived from EW analysis, while abundances of elements with HFS V, Mn, and Co are derived from spectral synthesis (see Table 3 for details of lines used). Figure 5 shows the fit of the 5528 Å Mg I line in the three stars, highlighting the difference in Mg abundance between the stars, especially for Tuc V-2 and Tuc V-3. We derive Ti abundances from both neutral and ionized Ti lines and find abundances in agreement within the uncertainties for all three stars, similarly for the Cr I and Cr II abundances in Tuc V-2. As can be seen in Figure 2, the α and iron-peak element abundances in Tuc V mostly follow the results from other UFD galaxies, except for Mn, which is very low in all the Tuc V stars. The Mn abundances in all three stars are derived from the Mn triplet around 4030 Å, which is known to result in lower abundances compared to other Mn lines (Cayrel et al. 2004; Sneden et al. 2023). Unfortunately, no other Mn lines were present in the spectra, supporting the low Mn abundances derived for the stars. A few other notable outliers are the high $[\text{Si}/\text{Fe}]$ in the CEMP star, Tuc V-1, and the high $[\text{Ca}/\text{Fe}]$ in Tuc V-3.

Table 4
Abundance Summary for the Three Tuc V Stars

Species	Tuc V-1					Tuc V-2					Tuc V-3							
	<i>N</i>	$\log \epsilon$ (X)	[X/H]	$\sigma_{[X/H]}$ (dex)	[X/Fe]	$\sigma_{[X/Fe]}$ (dex)	<i>N</i>	$\log \epsilon$ (X)	[X/H]	$\sigma_{[X/H]}$ (dex)	[X/Fe]	$\sigma_{[X/Fe]}$ (dex)	<i>N</i>	$\log \epsilon$ (X)	[X/H]	$\sigma_{[X/H]}$ (dex)	[X/Fe]	$\sigma_{[X/Fe]}$ (dex)
C–H	...	+5.99	-2.44	0.13	+1.11	0.11	...	+5.56	-2.87	0.10	-0.40	0.09	...	+6.10	-2.33	0.17	+0.29	0.15
C _{corr}	...	+6.65	-1.78	0.13	+1.77	0.11	...	+6.06	-2.37	0.10	+0.10	0.09	...	+6.37	-2.05	0.17	+0.56	0.15
C–N	...	+6.09	-1.75	0.35	+1.81	0.34
O I	3	+7.46	-1.23	0.26	+2.32	0.27
Na I	4	+3.64	-2.60	0.15	+0.95	0.15	5	+4.62	-1.62	0.10	+0.84	0.10	2	+3.77	-2.47	0.23	+0.14	0.21
Mg I	6	+5.41	-2.19	0.10	+1.36	0.11	8	+5.92	-1.68	0.09	+0.78	0.10	5	+5.09	-2.51	0.11	+0.10	0.12
Al I	1	+2.90	-3.55	0.45	0.00	0.45	1	+3.73	-2.72	0.41	-0.25	0.40	1	+3.06	-3.39	0.62	-0.78	0.62
Si I	1	+4.99	-2.52	0.22	+1.03	0.23	2	+5.07	-2.44	0.20	+0.02	0.19	2	+5.34	-2.17	0.32	+0.44	0.30
K I	2	+2.25	-2.78	0.11	+0.77	0.11	2	+3.23	-1.80	0.12	+0.66	0.11	1	+3.41	-1.62	0.16	+0.99	0.15
Ca I	16	+3.26	-3.08	0.09	+0.47	0.09	15	+4.37	-1.97	0.08	+0.49	0.08	15	+4.58	-1.76	0.11	+0.85	0.12
Sc II	7	-0.02	-3.17	0.14	+0.27	0.12	7	+0.84	-2.31	0.12	+0.13	0.10	5	+0.20	-2.96	0.19	-0.35	0.15
Ti I	4	+1.70	-3.25	0.16	+0.30	0.15	14	+2.71	-2.24	0.12	+0.22	0.11	2	+2.47	-2.48	0.20	+0.13	0.19
Ti II	16	+1.63	-3.32	0.15	+0.12	0.10	16	+2.73	-2.22	0.13	+0.22	0.11	12	+2.58	-2.37	0.15	+0.25	0.14
V II	...	<+1.11	<-2.82	...	<+0.62	...	1	+1.58	-2.35	0.16	+0.08	0.16	...	<+2.05	<-1.88	...	<+0.69	...
Cr I	2	+1.93	-3.71	0.19	-0.16	0.19	10	+3.00	-2.64	0.12	-0.18	0.11	6	+2.83	-2.81	0.17	-0.20	0.16
Cr II	2	+3.08	-2.56	0.17	-0.12	0.16	
Mn I	2	+0.71	-4.72	0.26	-1.17	0.25	3	+1.78	-3.65	0.21	-1.19	0.20	3	+1.58	-3.85	0.28	-1.23	0.28
Fe I	68	+3.95	-3.55	0.08	112	+5.04	-2.46	0.06	65	+4.89	-2.61	0.10
Fe II	4	+4.06	-3.44	0.13	11	+5.06	-2.44	0.10	6	+4.89	-2.61	0.14
Co I	3	+1.55	-3.48	0.20	+0.08	0.18	3	+2.16	-2.83	0.22	-0.37	0.21	2	+2.26	-2.73	0.29	-0.12	0.28
Ni I	...	<+3.09	<-3.10	...	<+0.32	...	6	+3.86	-2.36	0.11	+0.11	0.10	...	<+4.11	<-2.11	...	<+0.46	...
Zn I	...	<+1.92	<-2.64	...	<+0.80	...	2	+2.47	-2.09	0.13	+0.37	0.13	...	<+2.54	<-2.02	...	<+0.55	...
Sr II	2	-2.30	-5.17	0.18	-1.73	0.16	2	-0.82	-3.69	0.31	-1.26	0.27	1	-1.48	-4.35	0.38	-1.74	0.35
Y II	3	-0.91	-3.12	0.22	-0.69	0.21	
Zr II	1	-0.50	-3.08	0.35	-0.65	0.35	
Ba II	4	-2.48	-4.66	0.20	-1.22	0.16	5	-0.58	-2.76	0.15	-0.32	0.11	2	-1.44	-3.62	0.27	-1.01	0.23
La II	2	-1.55	-2.65	0.20	-0.22	0.19	
Ce II	2	-0.81	-2.39	0.31	+0.04	0.32	
Pr II	1	-1.34	-2.06	0.30	+0.37	0.27	
Nd II	5	-0.58	-2.00	0.13	+0.43	0.12	
Eu II	...	<-2.87	<-3.39	...	<+0.05	...	2	-1.53	-2.05	0.14	+0.36	0.11	...	<-1.54	<-2.06	...	<+0.51	...
Dy II	1	-1.16	-2.26	0.35	+0.18	0.36	

Table 5
Abundance Uncertainties

ID	El.	$\Delta_{T_{\text{eff}}}$ (dex)	$\Delta_{\log g}$ (dex)	Δ_{ξ} (dex)	$\Delta_{[\text{Fe}/\text{H}]}$ (dex)	s_{X} (dex)
Tuc V-1	C-H	0.10	-0.07	-0.01	0.03	0.07
Tuc V-1	C-N	0.20	-0.02	0.00	0.04	0.00
Tuc V-1	O I	-0.07	0.10	-0.01	0.01	0.43
Tuc V-1	Na I	0.09	-0.05	-0.03	-0.03	0.21
Tuc V-1	Mg I	0.08	-0.10	-0.06	-0.03	0.17
Tuc V-1	Al I	0.15	-0.13	-0.13	-0.08	0.30
Tuc V-1	Si I	-0.02	-0.06	-0.07	-0.05	0.00
Tuc V-1	K I	0.10	-0.03	-0.01	-0.02	0.00
Tuc V-1	Ca I	0.09	-0.04	-0.01	-0.02	0.09
Tuc V-1	Sc II	-0.01	0.08	-0.04	0.00	0.20
Tuc V-1	Ti I	0.16	-0.05	-0.01	-0.02	0.10
Tuc V-1	Ti II	0.04	0.07	-0.03	0.02	0.13
Tuc V-1	Cr I	0.14	-0.05	-0.02	-0.03	0.19
Tuc V-1	Mn I	0.23	-0.10	-0.05	-0.04	0.15
Tuc V-1	Fe I	0.08	-0.02	0.03	0.01	0.21
Tuc V-1	Fe II	0.00	0.09	-0.02	0.02	0.11
Tuc V-1	Co I	0.16	-0.06	-0.05	-0.04	0.09
Tuc V-1	Sr II	-0.02	0.07	-0.07	-0.01	0.00
Tuc V-1	Ba II	0.06	0.08	-0.00	0.03	0.19

(This table is available in its entirety in machine-readable form.)

4.3. Neutron-capture Elements

All abundances of neutron-capture elements are derived from spectral synthesis. For Tuc V-1 and Tuc V-3, we could only derive abundances for Sr and Ba. Both stars exhibit very low [Sr/Fe] and [Ba/Fe] ratios characteristic of UFD galaxy stars (Ji et al. 2019b) and labeling Tuc V-1 as a CEMP-no star ($[\text{Ba}/\text{Fe}] < 0$; Beers & Christlieb 2005). For Tuc V-2, however, due to a small enhancement in neutron-capture elements, abundances for Sr, Y, Zr, Ba, La, Pr, Nd, Eu, and Dy could also be derived. The spectral synthesis of the 4554 Å Ba II in all three stars is shown in Figure 6, where the higher neutron-capture element abundance of Tuc V-2 is clearly visible. Synthesis of additional neutron-capture element lines in Tuc V-2 is shown in Figure B1.

5. Discussion

5.1. Nature of Tuc V

The generally accepted criteria for distinguishing dwarf galaxies from globular clusters include direct dynamical evidence for dark matter from stellar kinematics and indirect evidence for dark matter based on a potential well deep enough to retain supernova (SN) ejecta, leading to a substantial spread in iron abundance among member stars (Willman & Strader 2012). Although the stellar kinematics of Tuc V do not place meaningful constraints on its dynamical mass (Simon et al. 2020), the chemical abundance measurements presented above clearly establish that Tuc V is a galaxy. Its stars span a metallicity range from $[\text{Fe}/\text{H}] = -3.55$ to $[\text{Fe}/\text{H}] = -2.46$, much larger than has been seen in any faint cluster (and extending to lower metallicities than known clusters). Other heavy elements such as Ca also vary by more than 1 dex within Tuc V, further supporting the system's ability to hold on to SN ejecta. The detailed abundances of Tuc V also resemble those of dwarf galaxies much more than globular clusters: the neutron-capture abundances are very low in two of the three

stars ($[\text{Sr}/\text{Fe}] < -1.5$, $[\text{Ba}/\text{Fe}] < -1$; Ji et al. 2019b), the K abundances are high (Webber et al. 2023), and CEMP-no stars have not been identified in clusters. Finally, we note that the metallicities of the Tuc V stars extend well below any known SMC stars, and the *r*-process abundances are lower than those of the most metal-poor stars in the SMC as well (Reggiani et al. 2021). These results argue strongly against the SMC origin suggested by Conn et al. (2018), as already concluded by Simon et al. (2020) based on the velocity of Tuc V.

With the updated sample of five member stars (four of which have metallicity measurements), we can also redetermine the bulk properties of Tuc V. Using the methodology from Li et al. (2017), we compute a mean metallicity of $[\text{Fe}/\text{H}] = -2.84^{+0.32}_{-0.30}$, with a metallicity spread of $\sigma_{[\text{Fe}/\text{H}]} = 0.43^{+0.32}_{-0.15}$. This revised metallicity places Tuc V close to the stellar mass–metallicity relationship for dwarf galaxies (e.g., Kirby et al. 2013b). Both the metallicity and metallicity spread are in agreement with the photometric measurements of a sample of six Tuc V stars by Fu et al. (2023). Using mean velocities for Tuc V-2 and Tuc V-3, as well as the center-of-mass velocity from the TheJoker Markov Chain Monte Carlo (MCMC) fit for Tuc V-1 (Section 5.2.1), the systemic velocity for Tuc V is $-34.7^{+0.9}_{-0.8} \text{ km s}^{-1}$, and the velocity dispersion is $\sigma = 1.2^{+0.9}_{-0.6} \text{ km s}^{-1}$. The velocity dispersion is only marginally resolved, and we compute 90% (95.5%) upper limits of 2.5 (3.1) km s^{-1} . These values are generally consistent with, but significantly more precise than, the results of Simon et al. (2020); the mean metallicity differs by more than 2σ , but since the original determination relied on only two stars, the uncertainty may have been underestimated.

5.2. CEMP-no Stars in UFD Galaxies

The most metal-poor star in the sample, Tuc V-1, can be classified as a CEMP-no star (Beers & Christlieb 2005), with significant enhancements in C ($[\text{C}/\text{Fe}] = 1.77$), N ($[\text{N}/\text{Fe}] = 1.81$), and O ($[\text{O}/\text{Fe}] = 2.32$) but low abundances of the neutron-capture elements Sr ($[\text{Sr}/\text{Fe}] = -1.73$) and Ba ($[\text{Ba}/\text{Fe}] = -1.22$). In Figure 3, we show the synthesis of the C-H *G* band in three sample stars. Ji et al. (2020b) compared the fraction of CEMP stars in UFD galaxies at $[\text{Fe}/\text{H}] < -2$ to that of the MW halo from Placco et al. (2014). They found that these are essentially identical, around 40%, while Skúladóttir et al. (2024) found a much lower fraction of CEMP stars of 9% below $[\text{Fe}/\text{H}] = -3$ in the classical dwarf spheroidal (dSph) galaxy Sculptor.

Tuc V-1 also exhibits substantial enhancements in the light elements Na, Mg, and Si, a signature detected in a subset of both the MW halo and UFD CEMP-no stars (e.g., Norris et al. 2013; Spite et al. 2018; Hayes et al. 2023) and, despite the potentially lower fractions of CEMP stars, also in dSph galaxies (Hansen et al. 2023; Roederer et al. 2023). The origin of the peculiar abundance pattern of the CEMP-no stars (both with and without the additional light-element enhancement) is still unknown. It has been suggested that this chemical signature can be produced by massive Population III stars ending their lives in low-energy or faint SNe with varying degrees of mixing and fallback (e.g., Umeda & Nomoto 2003; Iwamoto et al. 2005; Nomoto et al. 2013; Ishigaki et al. 2014). Another proposed source is fast-rotating massive metal-free stars, so-called spinstars (Meynet et al. 2006; Liu et al. 2021). Models of spinstars, which include extensive processing and mixing, can reproduce the additional light-element enhancement (Maeder & Meynet 2015). More recent theoretical work

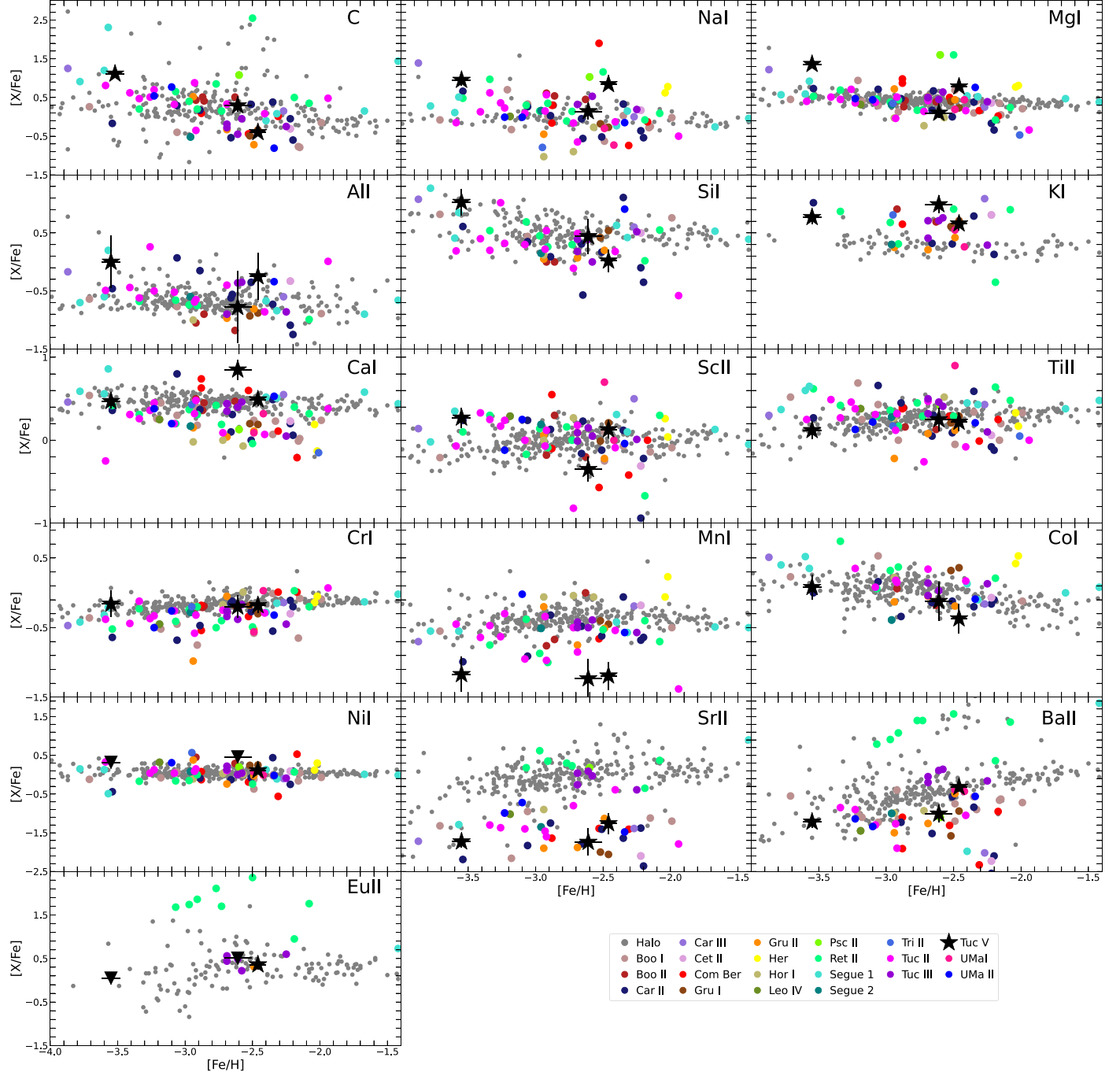


Figure 2. [X/Fe] derived abundances for Tuc V (black stars) compared to stellar abundances from the MW halo (gray dots; Roederer & Kirby 2014) and other UFD galaxies (colored dots according to legend; see text for references). Upper limits for Tuc V stars are marked with downward-pointing black triangles.

also suggests that CEMP-no stars can form from gas enriched by Population II Type II SNe (Jeon et al. 2021) or asymptotic giant branch (AGB) stars (Sharma et al. 2019). In an attempt to characterize the progenitors of CEMP-no stars in UFD galaxies, Rossi et al. (2023) constructed a chemical evolution model aiming to match the metallicity distribution function of the Boötes I galaxy. In their model, they include Population III and Population II SNe and AGB stars as sources of C and find that CEMP-no stars with $A(C) \leq 6$ were likely formed from gas polluted by Population III SNe, whereas Population II SNe or Population II AGB stars were the primary source of C for stars with $A(C) \geq 6$.

The top panel of Figure 7 shows the $A(C)^{11}$ as a function of metallicity for the CEMP-no stars in UFD galaxies. In this plot, we include four stars from Ret II, which all have high Ba abundances and thus do not fulfill the $[Ba/Fe] < 0$ requirement for CEMP-no stars (Beers & Christlieb 2005). However, the Ba in these stars is likely of an r -process origin (Ji et al. 2016a, 2016c; Hayes et al. 2023) and thus not coupled to the C enhancement. Inspection of this plot shows that Population II SNe likely enriched most CEMP-no stars in UFD galaxies (purple shaded region), according to the model from Rossi

¹¹ $A(C)$ is corrected for depletion due to stellar evolution.

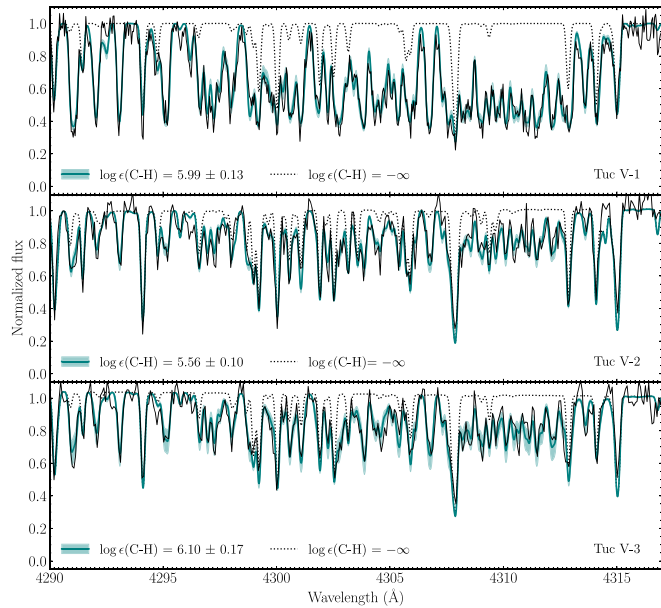


Figure 3. Comparison of synthesis and observed spectra (black line) for the C-H G -band in Tuc V-1 (top), Tuc V-2 (middle), and Tuc V-3 (bottom). The blue line is the best-fit synthesis, the blue band shows the uncertainty, and the dotted line is a synthesis without the given element.

et al. (2023). In principle, Population II AGB stars could also have polluted the gas from which these stars formed. However, since all of these stars have very low Ba abundances, $[\text{Ba}/\text{Fe}] < -0.5$,¹² these AGB stars would need to have a very low or nonexistent production of s -process elements, like Ba during the AGB phase.

Another test of the origin of CEMP-no stars can be made using the results from Hartwig et al. (2018), who argued that the $[\text{Mg}/\text{C}]$ ratio of stars could be used to determine if metal-poor stars have been enriched by single (mono-enriched) or multiple (multi-enriched) progenitors, where stars with $[\text{Mg}/\text{C}] < -1$ are most likely to be mono-enriched. In the bottom panel of Figure 7, we plot $[\text{Mg}/\text{C}_{\text{corr}}]$ as a function of metallicity for the UFD galaxy CEMP-no stars, and a dashed line separates the areas in this abundance space where the probability of stars being mono-enriched is $>50\%$ (cyan shaded region) and $<50\%$ (purple shaded region), adapted from Figure 11 in Hartwig et al. (2018). As can be seen, the models from Hartwig et al. (2018) and Rossi et al. (2023) largely agree on the fraction of stars enriched by Population II SNe (multi-enriched) and by Population III SNe (mono-enriched). However, the two methods somewhat disagree on which exact stars are likely mono-enriched. The highly C-enhanced star in Seg 1 highlights the divergence of the models, suggesting that using just C as a measure for enrichment might not be sufficient. It should be mentioned, though, that neither Hartwig et al. (2018) nor Rossi et al. (2023) include spinstars as a source of C and Mg in their models. Hence, these objects still cannot be ruled out as possible progenitors of CEMP-no stars.

5.2.1. Binarity of Tuc V-1

As mentioned in Section 2, Tuc V-1 is part of a binary system. To determine the orbital parameters of this system, we

fit the velocity data listed in Table 1 using the rejection sampling algorithm TheJoker (Price-Whelan et al. 2017), the result of which is shown in Figure 8. TheJoker returned a likely period of ~ 380 days. In order to explore the likelihood around this solution more completely, we then carried out an MCMC fit to the orbital parameters using PyMC. Based on the results from TheJoker, we initialized the MCMC with a prior on the period that was flat between 320 and 405 days, and we set Gaussian priors on the velocity semiamplitude and center-of-mass velocity using the best-fit TheJoker values and increasing the standard deviation on each quantity by a factor of ~ 5 so as not to unduly restrict the parameter space. The posterior parameter distributions from the MCMC were $P = 381^{+5}_{-4}$ days, $e = 0.10^{+0.03}_{-0.10}$, $K = 11.0^{+0.8}_{-1.0} \text{ km s}^{-1}$, and $v_{\text{hel}} = -32.4^{+0.7}_{-0.8} \text{ km s}^{-1}$. The resulting binary mass function is $f = 0.05 \pm 0.01 M_{\odot}$, corresponding to a minimum companion mass of $0.4 M_{\odot}$. Depending on the unknown inclination angle of the system, this measurement is consistent with an M dwarf, a K dwarf, or a white dwarf companion star.

The fact that Tuc V-1 is part of a binary system introduces the possibility that mass transfer from a more massive evolved companion has altered the abundances of this star, being the source of the C enrichment. However, extensive radial velocity monitoring of CEMP-no stars in the halo has found the majority of these to be single (Starkenburg et al. 2014; Hansen et al. 2016). Thus, these stars likely inherited their chemical peculiarities from the cloud they formed from rather than through binary interaction. Still, there is some observational evidence suggesting that the binary fraction of CEMP-no stars in the halo and dSph galaxies is correlated with the C abundance, with stars in binary systems having higher absolute C abundances than single CEMP-no stars (Arentsen et al. 2019; Hansen et al. 2023).

One other UFD CEMP-no star, J033607 in Ret II, has been found to show radial velocity variations (Hayes et al. 2023; Ji et al. 2023). Of the remaining UFD galaxy CEMP-no stars, 12 do not show radial velocity variations (Frebel et al. 2010; Norris et al. 2010; Spite et al. 2018; Chiti et al. 2023; Ji et al. 2023), while seven do not have multiple velocities reported in the literature. Looking at the absolute C abundances, Tuc V-1 has $A(\text{C}) = 6.65$, and the Ret II binary star has $A(\text{C}) = 6.21$, which, when inspecting the top panel of Figure 7, places these two stars in the middle or lower end of the $A(\text{C})$ distribution for the UFD galaxy CEMP-no stars, thus not following the trend seen for the halo and dSph, where binary CEMP-no stars are found mostly at $A(\text{C}) > 7$ (Arentsen et al. 2019; Hansen et al. 2023).

5.3. The r -process in UFD Galaxies

The most metal-rich star in our sample, Tuc V-2, exhibits a small enhancement in some neutron-capture elements. It has $[\text{Eu}/\text{Fe}] = 0.36$ and $[\text{Ba}/\text{Fe}] = -0.32$, resulting in a Ba-to-Eu ratio of -0.68 , consistent with pollution by a rapid neutron-capture (r)-process (Sneden et al. 2008). In Figure 9, we plot the absolute neutron-capture element abundances derived for the star and compare them to the solar system r - and s -process abundance patterns scaled to the stellar Ba and Eu abundances, respectively. Looking at the heavy neutron-capture elements (Ba and up), it is clear from this figure that the r -process pattern best matches the data of the two, confirming the r -process origin of the neutron-capture elements detected in Tuc V-2. For the lighter elements Sr, Y, and Zr, the agreement with the solar

¹² Except for the Ret II stars as explained above.

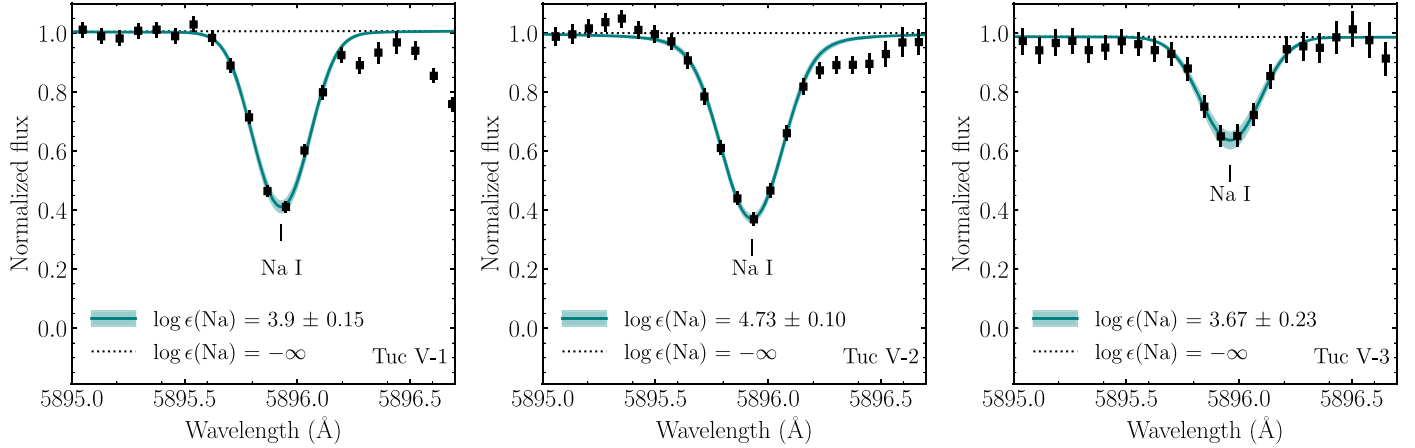


Figure 4. Comparison of synthesis and observed spectra (black squares) for the 5895 Å Na I line in Tuc V-1 (left), Tuc V-2 (middle), and Tuc V-3 (right). The blue line is the best-fit synthesis, the blue band shows the uncertainty, and the dotted line is a synthesis without the given element.

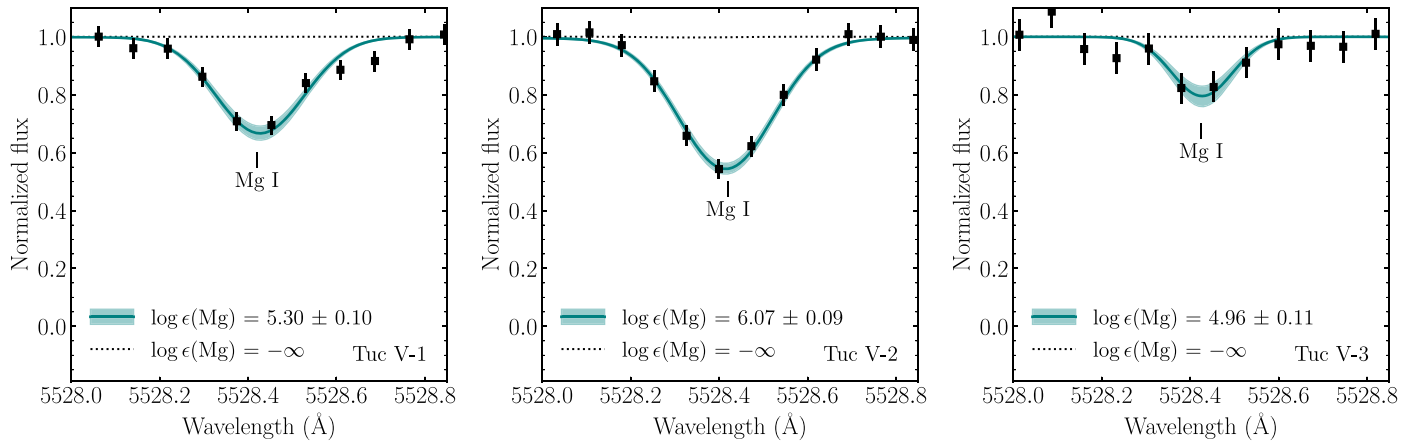


Figure 5. Comparison of synthesis and observed spectra (black squares) for the 5528 Å Mg I line in Tuc V-1 (left), Tuc V-2 (middle), and Tuc V-3 (right). The blue line is the best-fit synthesis, the blue band shows the uncertainty, and the dotted line is a synthesis without the given element.

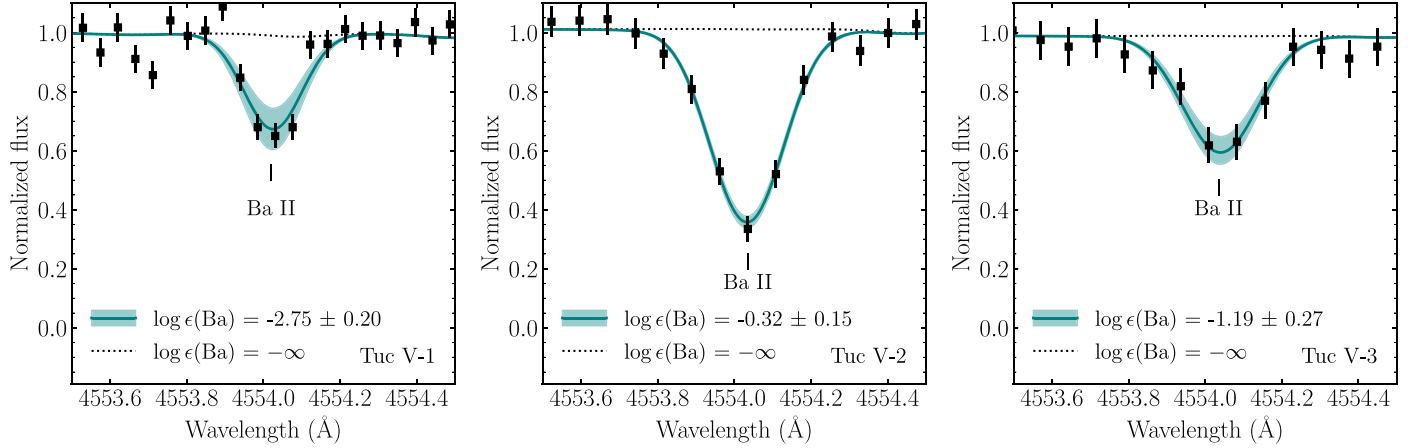


Figure 6. Comparison of synthesis and observed spectra (black squares) for the 4554 Å Ba II line in Tuc V-1 (left), Tuc V-2 (middle), and Tuc V-3 (right). The blue line is the best-fit synthesis, the blue band shows the uncertainty, and the dotted line is a synthesis without the given element.

pattern is less good; a similar signature has also been seen among MW halo *r*-process-enhanced stars and has been suggested to be the result of a limited *r*-process operating in this element range (McWilliam 1998; Hansen et al. 2012; Roederer et al. 2022).

r-process-enhanced stars have been found in three other UFD galaxies, with 72% of the stars analyzed in Reticulum II being highly *r*-process-enhanced (*r*-II stars; Ji et al. 2023), while the five stars analyzed in Tucana III and one star in Grus II are mildly enhanced ($0.22 < [\text{Eu}/\text{Fe}] < 0.60$) and

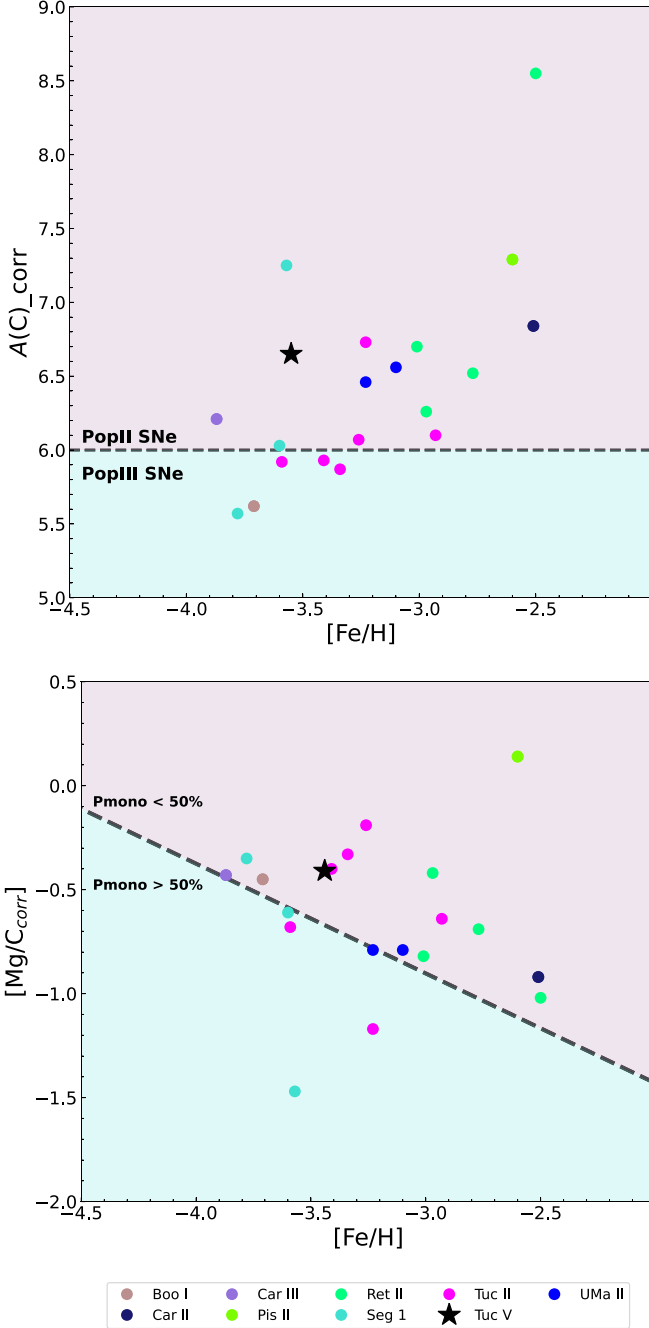


Figure 7. Top: absolute C abundances as a function of metallicity for the CEMP-no stars identified in UFD galaxies. The gray dashed line at $A(C) = 6$ marks the division between enrichment by Population II SNe or AGB stars ($A(C) > 6$) and Population III SNe ($A(C) < 6$) according to the Rossi et al. (2023) model. In this picture, most of the UFD CEMP-no stars, including Tuc V-1, have $A(C)$ values consistent with enrichment by Population II SNe or AGB stars. Bottom: $[\text{Mg}/\text{C}_{\text{corr}}]$ as a function of metallicity for the UFD galaxy CEMP-no stars. The dashed line separates areas in this abundance space where the probability of stars being mono-enriched is $>50\%$ and $<50\%$, adapted from Figure 11 in Hartwig et al. (2018). According to this metric, the gas from which most of the CEMP-no stars in UFD galaxies, including Tuc V-1, formed was enriched by multiple progenitors.

labeled r -I stars (Hansen et al. 2017, 2020; Marshall et al. 2019).

The astrophysical site(s) of the r -process is still debated, but currently only neutron star mergers (NSMs) have been observationally confirmed as an r -process element production site with the GW170817 event (Chornock et al. 2017; Drout

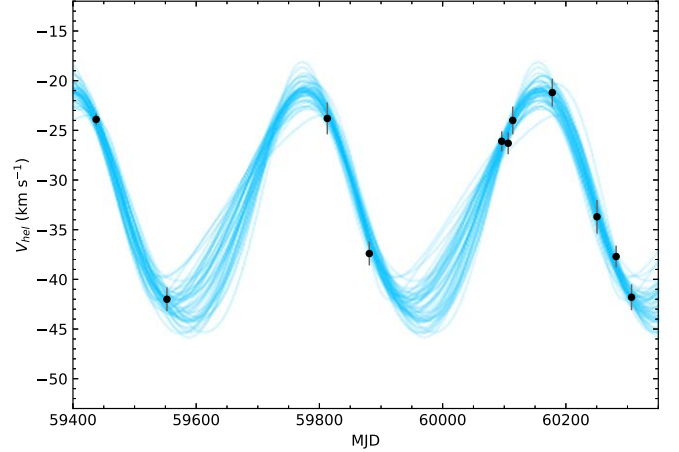


Figure 8. Radial velocity measurements for Tuc V-1 over the ~ 2 yr since our initial observation. The blue lines show a randomly selected set of MCMC samples that fit the velocity data.

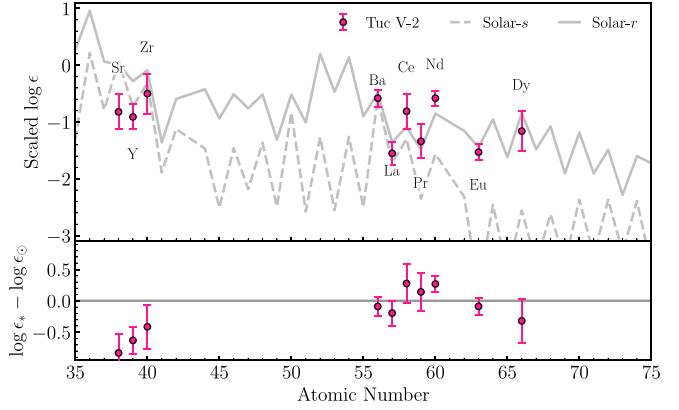


Figure 9. Absolute abundances for neutron-capture elements derived for Tuc V-2 compared to scaled solar system r - (solid) and s -process (dashed) abundances taken from Sneden et al. (2008). The stellar abundances most closely match the solar system r -process abundance pattern.

et al. 2017; Pian et al. 2017; Tanvir et al. 2017), although other sites, including various exotic SNe, have been proposed (Winteler et al. 2012; Mösta et al. 2018; Grichener & Soker 2019; Siegel et al. 2019). However, the lanthanide fraction of the material produced in GW170817 has been shown not to agree with the lanthanide fraction of the most r -process-enriched MW halo and UFD galaxy stars, with the ejecta from GW170817 not being lanthanide-rich enough to match the composition found in the stars (Ji et al. 2019a).

Currently, different NSM models predict different ejecta compositions. For example, models from Eichler et al. (2015) and Lippuner et al. (2017) find the dynamical ejecta to be neutron-rich, producing a high lanthanide fraction, whereas wind ejecta, for example, from an accretion disk, contributes more of the light r -process elements (below the second peak), while in models from Radice et al. (2018), r -process material with $90 < A < 125$ is also produced in the dynamical ejecta, depending on the total mass of the neutron stars and the equation of state. For GW170817, most of the ejected material came from the postmerger accretion disk (Siegel 2019, and references therein), suggesting that mergers with dynamical ejecta constituting a larger fraction of the total ejecta mass might be needed to match the stellar abundances.

A simple way to investigate the ratio of lanthanide-poor to lanthanide-rich material is by looking at the [Sr/Eu] ratios of the stars. For Tuc V-2, we measure $[\text{Sr/Eu}] = -1.62$, very similar to the value for the *r*-I star in Gru II ($[\text{Sr/Eu}] = -1.44$) and the average of the seven *r*-II stars in Ret II ($[\text{Sr/Eu}] = -1.44$), while the average value for the five *r*-I stars in Tuc III is somewhat higher at $[\text{Sr/Eu}] = -0.58$. The fairly consistent values found for Gru II, Ret II, and Tuc V could suggest that the (potential) NSMs polluting these galaxies shared some characteristics.

Holmbeck et al. (2021) used the [Zr/Dy] ratios of *r*-process-enhanced MW halo stars to backward-model the properties of the NSMs required to create the measured abundance ratios. They found that asymmetric systems ($M_1 \ll M_2$), which have higher dynamical ejecta mass, were generally needed to reproduce the lowest [Zr/Dy] ratios, which are equivalent to the low [Sr/Eu] derived for the Gru II, Ret II, and Tuc V *r*-process-enhanced stars.

The time delay connected to the NSM scenario, however, still introduces a problem with this enrichment channel. For example, for Ret II, the large fraction of *r*-process-enriched stars combined with the star formation history of the galaxy (Simon et al. 2023) led Ji et al. (2023) to suggest that a rare type of core-collapse SN is more likely the source of the *r*-process material in this galaxy than an NSM. In both Gru II and Tuc V, it is the most metal-rich star in the sample that exhibits the *r*-process enrichment, suggesting that the *r*-process production occurred after a delay, late in the star formation process in these galaxies. The analysis of future larger samples of stars in these two systems providing information on the overall *r*-process enhancement level of the galaxies and their star formation histories, like in Ret II, will reveal more about their *r*-process element polluters.

5.4. Chemical Diversity in UFD Galaxies

The three Tuc V stars analyzed in this paper present very diverse sets of chemical compositions. In addition to the carbon and *r*-process enrichment discussed above, the three stars in Tuc V span a remarkably wide range in their Mg-to-Ca ratios with $[\text{Mg/Ca}] = 0.89$ (Tuc V-1), $[\text{Mg/Ca}] = 0.29$ (Tuc V-2), and $[\text{Mg/Ca}] = -0.75$ (Tuc V-3). Excluding the CEMP-no star (Tuc V-1), where the high $[\text{Mg/Fe}]$ value is likely coupled to its C enhancement, the [Mg/Ca] ratios for the other two stars still differ by 1.04 dex despite their similar metallicities, which suggest a decoupling between the Fe and α enrichment of the stars. Furthermore, such large variations in enrichment, especially among stars with similar metallicities, imply that the interstellar medium of Tuc V must have been highly inhomogeneous and, correspondingly, that the number of SNe responsible for the chemical enrichment must have been small.

Ranges in [Mg/Ca] ratios in UFD galaxy stars are usually interpreted as a consequence of core-collapse SNe of varying masses enriching in the galaxy (Hansen et al. 2020; Ji et al. 2020a). However, Type Ia SNe are also known to produce significant amounts of Ca (Kobayashi et al. 2020). Hence, a low [Mg/Ca] ratio can also be the signature of enrichment by a Type Ia SN.

Disregarding CEMP-no stars with large enhancements in light elements, the only other UFD galaxy displaying a similar range in [Mg/Ca] values is Tuc II, with a range of 1.37 dex, driven by two of the new members discovered in the outskirts of the galaxy and analyzed by Chiti et al. (2023). Chiti et al.

(2023) argue that Tuc II was mainly enriched by low-energy core-collapse SNe owing to the large fraction of CEMP stars in the galaxy. Still, they also find evidence for enrichment by a sub-Chandrasekhar-mass Type Ia SN in the most metal-rich star in their sample. This star is also the one with the lowest [Mg/Ca] ratio of -0.72 in their sample, and they argue that some of the Ca in this star likely comes from the Type Ia SN, as Ca does not follow the trend of the other α -elements in this star.

The low [Mg/Ca] ratio found for Tuc V-3 in this analysis is mainly driven by a high [Ca/Fe]. This could suggest that Tuc V-3 has been enriched by a Type Ia SN and possibly also a sub-Chandrasekhar-mass Type Ia SN, as no significant difference is seen between this star and the other two stars for other elements expected to show signatures of Type Ia enrichment like Cr, Mn, and Ni (Kobayashi et al. 2020).

Finally, it has also been suggested that the [Mg/Ca] ratios of stars in UFD galaxies are coupled to the environment of the galaxy where UFD galaxies associated with the Large Magellanic Clouds (LMC) display a correlation between [Mg/Ca] and metallicity. With the sample of stars analyzed in this work, it is not possible to determine if a trend is present for [Mg/Ca] in Tuc V. However, the orbit of Tuc V does not indicate that it is a satellite of the LMC (Simon et al. 2020).

6. Summary

We present a detailed chemical analysis of three stars in the Tuc V system. In addition to a bright, known member in the center of the galaxy, Tuc V-3, we have identified two new members, Tuc V-1 and Tuc V-2, in the outskirts of the galaxy from Gaia astrometry. We then use the abundances to investigate the nature and chemical enrichment of the system. The large scatter between the stars detected for abundances of elements like Mg, Ca, Sc, and Fe tells us that Tuc V is a UFD galaxy with a very inhomogeneous chemical enrichment history. It holds both an *r*-I star (Tuc V-2) and a CEMP-no star (Tuc V-1). The C and Mg abundances of the CEMP-no star combined with C and Mg abundances from all known CEMP-no stars in UFD galaxies suggest that the majority of these have experienced enrichment from multiple progenitors. The [Sr/Eu] ratio of the *r*-I star points to an *r*-process element source that shares characteristics with the sources enriching Gru II and Ret II. Finally, we detect a very wide range in the [Mg/Ca] ratios of the stars. A similar range is only seen in one other UFD galaxy, namely, Tuc II, where the Mg and Ca abundances of stars located some distance from the center drive this diversity. Hence, obtaining the abundances of stars both in the center and in the outskirts of these galaxies is needed to fully assess their chemical diversity.

Acknowledgments

The authors thank the referee, Dr. Ricardo Schiavon, for the careful read of the paper and useful comments, which have improved the manuscript. T.T.H. acknowledges support from the Swedish Research Council (VR 2021-05556). A.P.J. acknowledges support by the National Science Foundation under grants AST-2206264 and AST-2307599. T.S.L. acknowledges financial support from the Natural Sciences and Engineering Research Council of Canada (NSERC) through grant RGPIN-2022-04794. J.Y.G. acknowledges support from a Carnegie Fellowship. This paper includes data

gathered with the 6.5 m Magellan Telescopes located at Las Campanas Observatory. This research made extensive use of the SIMBAD database operated at CDS, Strasbourg, France (Wenger et al. 2000), <https://arxiv.org/>, and NASA's Astrophysics Data System for bibliographic information. We thank Adrian Price-Whelan for assistance with binary fitting using TheJoker.

This work has made use of data from the European Space Agency (ESA) mission Gaia (<https://www.cosmos.esa.int/gaia>), processed by the Gaia Data Processing and Analysis Consortium (DPAC; <https://www.cosmos.esa.int/web/gaia/dpac/consortium>). Funding for the DPAC has been provided by national institutions, in particular, the institutions participating in the Gaia Multilateral Agreement.

This project used public archival data from the Dark Energy Survey (DES). Funding for the DES Projects has been provided by the U.S. Department of Energy, the U.S. National Science Foundation, the Ministry of Science and Education of Spain, the Science and Technology Facilities Council of the United Kingdom, the Higher Education Funding Council for England, the National Center for Supercomputing Applications at the University of Illinois at Urbana-Champaign, the Kavli Institute of Cosmological Physics at the University of Chicago, the Center for Cosmology and Astro-Particle Physics at the Ohio State University, the Mitchell Institute for Fundamental Physics and Astronomy at Texas A&M University, Financiadora de Estudos e Projetos, Fundação Carlos Chagas Filho de Amparo à Pesquisa do Estado do Rio de Janeiro, Conselho Nacional de Desenvolvimento Científico e Tecnológico and the Ministério da Ciência, Tecnologia e Inovação, the Deutsche Forschungsgemeinschaft, and the Collaborating Institutions in the Dark Energy Survey. The Collaborating Institutions are Argonne National Laboratory, the University of California at Santa Cruz, the University of Cambridge, Centro de Investigaciones Energéticas, Medioambientales y Tecnológicas-Madrid, the University of Chicago, University College London, the DES-Brazil Consortium, the University of Edinburgh, the Eidgenössische Technische Hochschule (ETH) Zürich, Fermi National Accelerator

Laboratory, the University of Illinois at Urbana-Champaign, the Institut de Ciències de l'Espai (IEEC/CSIC), the Institut de Física d'Altes Energies, Lawrence Berkeley National Laboratory, the Ludwig-Maximilians Universität München and the associated Excellence Cluster Universe, the University of Michigan, the National Optical Astronomy Observatory, the University of Nottingham, The Ohio State University, the OzDES Membership Consortium, the University of Pennsylvania, the University of Portsmouth, SLAC National Accelerator Laboratory, Stanford University, the University of Sussex, and Texas A&M University. Based in part on observations at Cerro Tololo Inter-American Observatory, National Optical Astronomy Observatory, which is operated by the Association of Universities for Research in Astronomy (AURA) under a cooperative agreement with the National Science Foundation.

Facilities: Magellan:Clay, Magellan:Baade.

Software: MOOG (Sneden 1973; Sobeck et al. 2011), IRAF (Tody 1986, 1993), ATLAS9 (Castelli & Kurucz 2003), linemake (Placco et al. 2021), NumPy (van der Walt et al. 2011), Matplotlib (Hunter 2007), AstroPy (Astropy Collaboration et al. 2013, 2018), CarPy (Kelson 2003), SMHR (Casey 2014).

Appendix A Stellar Parameters

Temperatures used in this work are derived photometrically using the color- T_{eff} relations from Casagrande et al. (2010). In Table A1, we list temperatures derived from the individual color bands used along with spectroscopic temperatures of the stars corrected for the offset between spectroscopic and photometric temperature scales using the method outlined in Frebel et al. (2013). The uncertainty related to this correction is 150 K. Table A2 lists the stellar parameter uncertainties arising from the standard deviation of T_{eff} from the four colors used (photo) and the effect of the standard deviation of abundances of FeI lines used (stat) as described in Section 3. Stellar parameter diagnostic plots for the three stars are shown in Figure A1.

Table A1
Photometric Temperatures

ID	$T_{\text{eff}}(B - V)$ (K)	$T_{\text{eff}}(V - R)$ (K)	$T_{\text{eff}}(R - I)$ (K)	$T_{\text{eff}}(V - I)$ (K)	$T_{\text{eff}}(\text{spec})$ (K)
Tuc V-1	4287	4365	4512	4356	4481
Tuc V-2	4691	4766	4861	4776	4827
Tuc V-3	4961	4985	5015	4967	5164

Table A2
Stellar Parameter Uncertainties

Param.	Tuc V-1	Tuc V-2	Tuc V-3
$\Delta T_{\text{eff,photo}}$	94	70	24
$\Delta T_{\text{eff,stat}}$	45	60	128
$\Delta \log g_{\text{photo}}$	0.29	0.19	0.10
$\Delta \log g_{\text{stat}}$	0.14	0.10	0.17
$\Delta \xi_{\text{photo}}$	0.02	0.01	0.00
$\Delta \xi_{\text{stat}}$	0.09	0.07	0.13
$\Delta [\text{Fe}/\text{H}]_{\text{photo}}$	0.14	0.03	0.03
$\Delta [\text{Fe}/\text{H}]_{\text{stat}}$	0.15	0.15	0.25

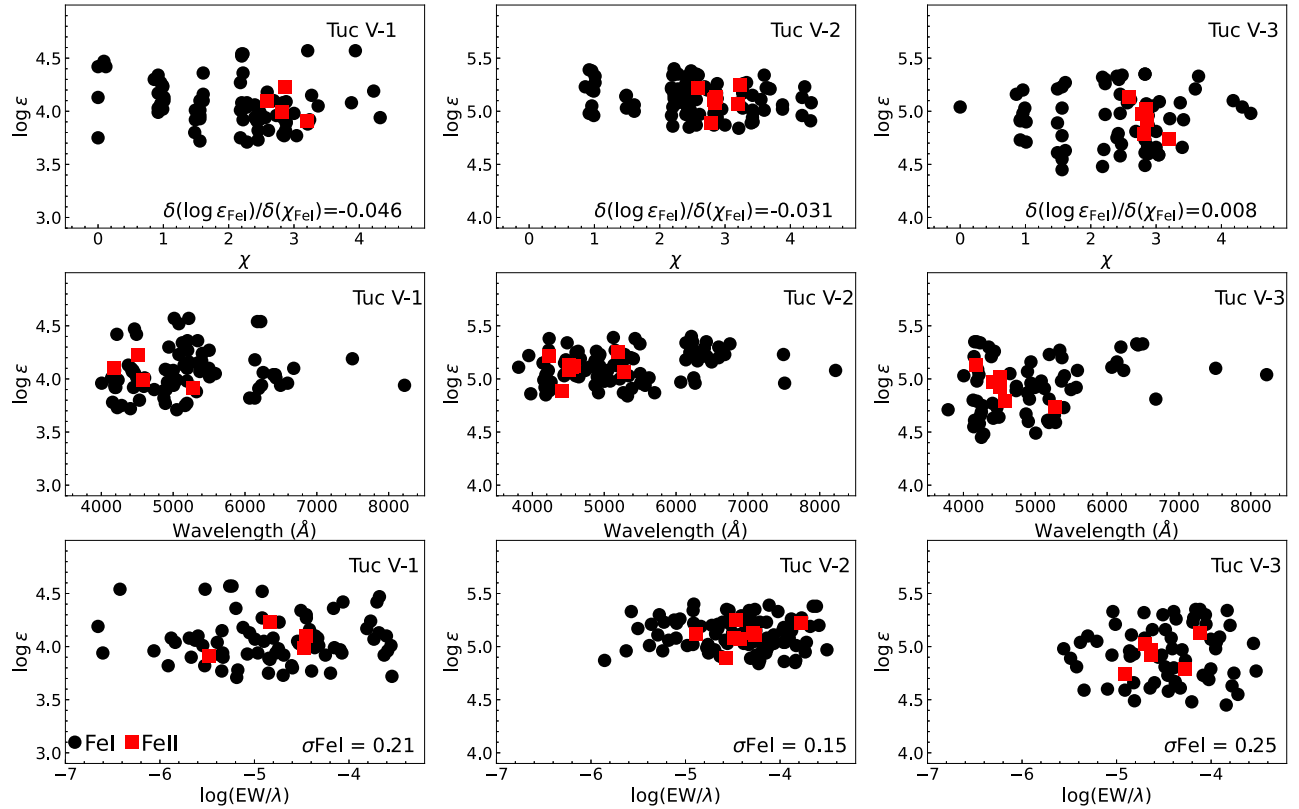


Figure A1. $\log \epsilon$ of Fe I and Fe II lines used for parameter determination of Tuc V-1 (left), Tuc V-2 (middle), and Tuc V-3 (right) as a function of excitation potential (top), wavelength (middle), and reduced EW (bottom).

Appendix B

Synthesis of Neutron-capture Elements

The synthesis of neutron-capture element absorption features in the spectrum of Tuc V-2 is shown in Figure B1.

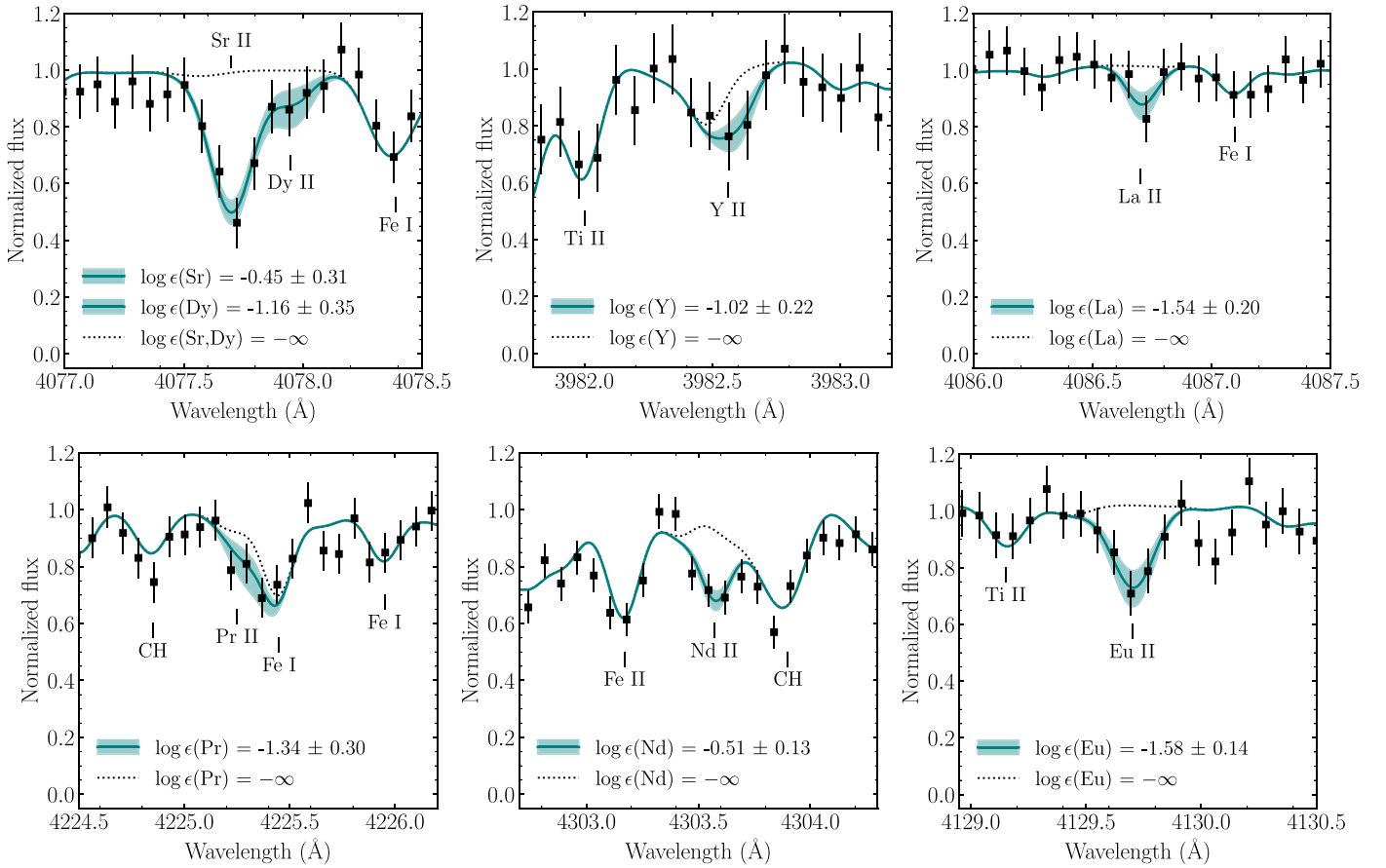


Figure B1. Comparison of synthesis and observed spectra (black squares) for neutron-capture elements in Tuc V-2. The blue line is the best-fit synthesis, the blue band shows the uncertainty, and the dotted line is a synthesis without the given element.

ORCID iDs

Terese T. Hansen <https://orcid.org/0000-0001-6154-8983>
 Joshua D. Simon <https://orcid.org/0000-0002-4733-4994>
 Ting S. Li <https://orcid.org/0000-0002-9110-6163>
 Alexander P. Ji <https://orcid.org/0000-0002-4863-8842>
 Henrique M. Reggiani <https://orcid.org/0000-0001-6533-6179>
 Jhon Yana Galarza <https://orcid.org/0000-0001-9261-8366>

References

Abbott, T. M. C., Abdalla, F. B., Allam, S., et al. 2018, *ApJS*, 239, 18
 Aoki, W., Beers, T. C., Christlieb, N., et al. 2007, *ApJ*, 655, 492
 Arentsen, A., Starkenburg, E., Shetrone, M. D., et al. 2019, *A&A*, 621, A108
 Asplund, M., Grevesse, N., Sauval, A. J., et al. 2009, *ARA&A*, 47, 481
 Astropy Collaboration, Price-Whelan, A. M., Sipőcz, B. M., et al. 2018, *AJ*, 156, 123
 Astropy Collaboration, Robitaille, T. P., Tollerud, E.J., et al. 2013, *A&A*, 558, A33
 Baumgardt, H., Faller, J., Meinholt, N., et al. 2022, *MNRAS*, 510, 3531
 Beers, T. C., & Christlieb, N. 2005, *ARA&A*, 43, 531
 Belmonte, M. T., Pickering, J. C., Ruffoni, M. P., et al. 2017, *ApJ*, 848, 125
 Bernstein, R., Shectman, S. A., Gunnels, S. M., et al. 2003, *Proc. SPIE*, 4841, 1694
 Biémont, É., Blagoev, K., Engström, L., et al. 2011, *MNRAS*, 414, 3350
 Blackwell, D. E., Shallis, M. J., & Simmons, G. J. 1982, *MNRAS*, 199, 33
 Bovy, J. 2015, *ApJS*, 216, 29
 Casagrande, L., Ramírez, I., Meléndez, J., et al. 2010, *A&A*, 512, A54
 Casey, A. R. 2014, PhD thesis, Australian National Univ.
 Castelli, F., & Kurucz, R. L. 2003, IAU Symp. 210, Modelling of Stellar Atmospheres, ed. N. Piskunov, W. W. Weiss, & D. F. Gray (San Francisco, CA: ASP), A20
 Cayrel, R., Depagne, E., Spite, M., et al. 2004, *A&A*, 416, 1117
 Chiti, A., Frebel, A., Ji, A. P., et al. 2018, *ApJ*, 857, 74
 Chiti, A., Frebel, A., Ji, A. P., et al. 2023, *AJ*, 165, 55
 Chiti, A., Frebel, A., Simon, J. D., et al. 2021, *NatAs*, 5, 392
 Chornock, R., Berger, E., Kasen, D., et al. 2017, *ApJL*, 848, L19
 Conn, B. C., Jerjen, H., Kim, D., et al. 2018, *ApJ*, 852, 68
 Den Hartog, E. A., Lawler, J. E., Sneden, C., et al. 2019, *ApJS*, 243, 33
 Den Hartog, E. A., Lawler, J. E., Sneden, C., et al. 2021, *ApJS*, 255, 27
 Den Hartog, E. A., Lawler, J. E., Sneden, C., et al. 2023, *ApJS*, 265, 42
 Den Hartog, E. A., Lawler, J. E., Sobeck, J. S., et al. 2011, *ApJS*, 194, 35
 Den Hartog, E. A., Ruffoni, M. P., Lawler, J. E., et al. 2014, *ApJS*, 215, 23
 Dotter, A., Chaboyer, B., Jevremović, D., et al. 2008, *ApJS*, 178, 89
 Dressler, A., Bigelow, B., Hare, T., et al. 2011, *PASP*, 123, 288
 Drlica-Wagner, A., Bechtol, K., Rykoff, E. S., et al. 2015, *ApJ*, 813, 109
 Drlica-Wagner, A., Sevilla-Noarbe, I., Rykoff, E. S., et al. 2018, *ApJS*, 235, 33
 Drout, M. R., Piro, A. L., Shappee, B. J., et al. 2017, *Sci*, 358, 1570
 Eichler, M., Arcones, A., Kelic, A., et al. 2015, *ApJ*, 808, 30
 Fadely, R., Willman, B., Geha, M., et al. 2011, *AJ*, 142, 88
 Feltzing, S., Eriksson, K., Kleyna, J., et al. 2009, *A&A*, 508, L1
 Filion, C., & Wyse, R. F. G. 2021, *ApJ*, 923, 218
 Frebel, A., Casey, A. R., Jacobson, H. R., et al. 2013, *ApJ*, 769, 57
 Frebel, A., Norris, J. E., Gilmore, G., et al. 2016, *ApJ*, 826, 110
 Frebel, A., Simon, J. D., Geha, M., et al. 2010, *ApJ*, 708, 560
 Frebel, A., Simon, J. D., & Kirby, E. N. 2014, *ApJ*, 786, 74
 Fu, S. W., Weisz, D. R., Starkenburg, E., et al. 2023, *ApJ*, 958, 167
 Gaia Collaboration, Brown, A. G. A., Vallenari, A., et al. 2021, *A&A*, 649, A1
 Gaia Collaboration, Prusti, T., de Bruijne, J. H. J., et al. 2016, *A&A*, 595, A1
 Geha, M., Willman, B., Simon, J. D., et al. 2009, *ApJ*, 692, 1464
 Gilmore, G., Norris, J. E., Monaco, L., et al. 2013, *ApJ*, 763, 61
 Goater, A., Read, J. I., Noël, N. E. D., et al. 2024, *MNRAS*, 527, 2403
 Grichener, A., & Soker, N. 2019, *ApJ*, 878, 24
 Hansen, C. J., Primas, F., Hartman, H., et al. 2012, *A&A*, 545, A31
 Hansen, T. T., Andersen, J., Nordström, B., et al. 2016, *A&A*, 586, A160
 Hansen, T. T., Marshall, J. L., Simon, J. D., et al. 2020, *ApJ*, 897, 183
 Hansen, T. T., Simon, J. D., Li, T. S., et al. 2023, *A&A*, 674, A180
 Hansen, T. T., Simon, J. D., Marshall, J. L., et al. 2017, *ApJ*, 838, 44
 Hartwig, T., Yoshida, N., Magg, M., et al. 2018, *MNRAS*, 478, 1795
 Hayes, C. R., Venn, K. A., Waller, F., et al. 2023, *ApJ*, 955, 17
 Holmbeck, E. M., Frebel, A., McLaughlin, G. C., et al. 2021, *ApJ*, 909, 21
 Hunter, J. D. 2007, *CSE*, 9, 90
 Ishigaki, M. N., Aoki, W., Arimoto, N., et al. 2014, *A&A*, 562, A146
 Ivans, I. I., Simmerer, J., Sneden, C., et al. 2006, *ApJ*, 645, 613
 Ivarsson, S., Litzén, U., & Wahlgren, G. M. 2001, *PhyS*, 64, 455
 Iwamoto, N., Umeda, H., Tominaga, N., et al. 2005, *Sci*, 309, 451
 Jeon, M., Bromm, V., Besla, G., et al. 2021, *MNRAS*, 502, 1
 Ji, A. P., Drout, M. R., & Hansen, T. T. 2019a, *ApJ*, 882, 40
 Ji, A. P., Frebel, A., Chiti, A., et al. 2016a, *Natur*, 531, 610
 Ji, A. P., Frebel, A., Ezzeddine, R., et al. 2016b, *ApJL*, 832, L3
 Ji, A. P., Frebel, A., Simon, J. D., et al. 2016c, *ApJ*, 830, 93
 Ji, A. P., Frebel, A., Simon, J. D., et al. 2016d, *ApJ*, 817, 41
 Ji, A. P., Li, T. S., Hansen, T. T., et al. 2020a, *AJ*, 160, 181
 Ji, A. P., Li, T. S., Simon, J. D., et al. 2020b, *ApJ*, 889, 27
 Ji, A. P., Simon, J. D., Frebel, A., et al. 2019b, *ApJ*, 870, 83
 Ji, A. P., Simon, J. D., Roederer, I. U., et al. 2023, *AJ*, 165, 100
 Kelson, D. D. 2003, *PASP*, 115, 688
 Kelson, D. D., Illingworth, G. D., van Dokkum, P. G., et al. 2000, *ApJ*, 531, 159
 Kim, D., Jerjen, H., Milone, A. P., et al. 2015, *ApJ*, 803, 63
 Kirby, E. N., Boylan-Kolchin, M., Cohen, J. G., et al. 2013a, *ApJ*, 770, 16
 Kirby, E. N., Cohen, J. G., Guhathakurta, P., et al. 2013b, *ApJ*, 779, 102
 Kobayashi, C., Karakas, A. I., & Lugaro, M. 2020, *ApJ*, 900, 179
 Koch, A., McWilliam, A., Grebel, E. K., et al. 2008, *ApJL*, 688, L13
 Kramida, A., Ralchenko, Y., Reader, J., & NIST ASD Team 2023, NIST Atomic Spectra Database (version 5.10) (Gaithersburg, MD: National Institute of Standards and Technology), <https://physics.nist.gov/asd>
 Lawler, J. E., Bonvallet, G., & Sneden, C. 2001a, *ApJ*, 556, 452
 Lawler, J. E., Guzman, A., Wood, M. P., et al. 2013, *ApJS*, 205, 11
 Lawler, J. E., Hala, Sneden, C., et al. 2019, *ApJS*, 241, 21
 Lawler, J. E., Sneden, C., Cowan, J. J., et al. 2009, *ApJS*, 182, 51
 Lawler, J. E., Sneden, C., & Cowan, J. J. 2015, *ApJS*, 220, 13
 Lawler, J. E., Sneden, C., Nave, G., et al. 2017, *ApJS*, 228, 10
 Lawler, J. E., Wickliffe, M. E., den Hartog, E. A., et al. 2001b, *ApJ*, 563, 1075
 Li, R., Chatelain, R., Holt, R. A., et al. 2007, *PhyS*, 76, 577
 Li, T. S., Simon, J. D., Drlica-Wagner, A., et al. 2017, *ApJ*, 838, 8
 Lippuner, J., Fernández, R., Roberts, L. F., et al. 2017, *MNRAS*, 472, 904
 Liu, B., Sibony, Y., Meynet, G., et al. 2021, *MNRAS*, 506, 5247
 Ljung, G., Nilsson, H., Asplund, M., et al. 2006, *A&A*, 456, 1181
 Longard, N., Jablonka, P., Arentsen, A., et al. 2022, *MNRAS*, 516, 2348
 Maeder, A., & Meynet, G. 2015, *A&A*, 580, A32
 Marshall, J. L., Hansen, T., Simon, J. D., et al. 2019, *ApJ*, 882, 177
 McWilliam, A. 1998, *AJ*, 115, 1640
 Meléndez, J., & Barbuy, B. 2009, *A&A*, 497, 611
 Meynet, G., Ekström, S., & Maeder, A. 2006, *A&A*, 447, 623
 Mörts, P., Roberts, L. F., Halevi, G., et al. 2018, *ApJ*, 864, 171
 Nagasawa, D. Q., Marshall, J. L., Li, T. S., et al. 2018, *ApJ*, 852, 99
 Nomoto, K., Kobayashi, C., & Tominaga, N. 2013, *ARA&A*, 51, 457
 Norris, J. E., Wyse, R. F. G., Gilmore, G., et al. 2010, *ApJ*, 723, 1632
 Norris, J. E., Yong, D., Bessell, M. S., et al. 2013, *ApJ*, 762, 28
 O'Brian, T. R., Wickliffe, M. E., Lawler, J. E., et al. 1991, *JOSAB*, 8, 1185
 Pace, A. B., Erkal, D., & Li, T. S. 2022, *ApJ*, 940, 136
 Pehlivan Rhodin, A., Hartman, H., Nilsson, H., et al. 2017, *A&A*, 598, A102
 Pian, E., D'Avanzo, P., Benetti, S., et al. 2017, *Natur*, 551, 67
 Pickering, J. C., Thorne, A. P., & Perez, R. 2001, *ApJS*, 132, 403
 Pickering, J. C., Thorne, A. P., & Perez, R. 2002, *ApJS*, 138, 247
 Placco, V. M., Frebel, A., Beers, T. C., et al. 2014, *ApJ*, 797, 21
 Placco, V. M., Sneden, C., Roederer, I. U., et al. 2021, *RNAAS*, 5, 92
 Price-Whelan, A. M., Hogg, D. W., Foreman-Mackey, D., et al. 2017, *ApJ*, 837, 20
 Radice, D., Perego, A., Hotokezaka, K., et al. 2018, *ApJ*, 869, 130
 Reggiani, H., Schlaufman, K. C., Casey, A. R., et al. 2021, *AJ*, 162, 229
 Roederer, I. U., Cowan, J. J., Pignatari, M., et al. 2022, *ApJ*, 936, 84
 Roederer, I. U., & Kirby, E. N. 2014, *MNRAS*, 440, 2665
 Roederer, I. U., & Lawler, J. E. 2012, *ApJ*, 750, 76
 Roederer, I. U., Pace, A. B., Placco, V. M., et al. 2023, *ApJ*, 954, 55
 Roederer, I. U., Preston, G. W., Thompson, I. B., et al. 2014, *AJ*, 147, 136
 Rossi, M., Salvadori, S., Skúladóttir, Á., et al. 2023, *MNRAS*, 522, L1
 Ruffoni, M. P., Den Hartog, E. A., Lawler, J. E., et al. 2014, *MNRAS*, 441, 3127
 Sharma, M., Theuns, T., & Frenk, C. 2019, *MNRAS*, 482, L145
 Shectman, S. A., & Johns, M. 2003, *Proc. SPIE*, 4837, 910
 Siegel, D. M. 2019, *EPJA*, 55, 203
 Siegel, D. M., Barnes, J., & Metzger, B. D. 2019, *Natur*, 569, 241
 Simon, J. D., Brown, T. M., Mutlu-Pakdil, B., et al. 2023, *ApJ*, 944, 43
 Simon, J. D., Frebel, A., McWilliam, A., et al. 2010, *ApJ*, 716, 446
 Simon, J. D., Geha, M., Minor, Q. E., et al. 2011, *ApJ*, 733, 46

Simon, J. D., Li, T. S., Drlica-Wagner, A., et al. 2017, *ApJ*, **838**, 11

Simon, J. D., Li, T. S., Erkal, D., et al. 2020, *ApJ*, **892**, 137

Skúladóttir, Á., Vanni, I., Salvadori, S., et al. 2024, *A&A*, **681**, A44

Sneden, C., Boesgaard, A. M., Cowan, J. J., et al. 2023, *ApJ*, **953**, 31

Sneden, C., Cowan, J. J., & Gallino, R. 2008, *ARA&A*, **46**, 241

Sneden, C., Lawler, J. E., Cowan, J. J., et al. 2009, *ApJS*, **182**, 80

Sneden, C. A. 1973, PhD thesis, The Univ. of Texas at Austin

Sobeck, J. S., Kraft, R. P., Sneden, C., et al. 2011, *AJ*, **141**, 175

Sobeck, J. S., Lawler, J. E., & Sneden, C. 2007, *ApJ*, **667**, 1267

Spite, M., Spite, F., François, P., et al. 2018, *A&A*, **617**, A56

Starkenburg, E., Shetrone, M. D., McConnachie, A. W., et al. 2014, *MNRAS*, **441**, 1217

Tanvir, N. R., Levan, A. J., González-Fernández, C., et al. 2017, *ApJL*, **848**, L27

Tarumi, Y., Yoshida, N., & Frebel, A. 2021, *ApJL*, **914**, L10

Tody, D. 1986, *Proc. SPIE*, **627**, 733

Tody, D. 1993, in ASP Conf. Ser. 173, Astronomical Data Analysis Software and Systems II, ed. R. J. Hanisch, R. J. V. Brissenden, & J. Barnes (San Francisco, CA: ASP), 173

Umeda, H., & Nomoto, K. 2003, *Natur*, **422**, 871

van der Walt, S., Colbert, S. C., & Varoquaux, G. 2011, *CSE*, **13**, 22

Waller, F., Venn, K. A., Sestito, F., et al. 2023, *MNRAS*, **519**, 1349

Webber, K. B., Hansen, T. T., Marshall, J. L., et al. 2023, *ApJ*, **959**, 141

Wenger, M., Ochsenbein, F., Egret, D., et al. 2000, *A&AS*, **143**, 9

Wickliffe, M. E., Lawler, J. E., & Nave, G. 2000, *JQSRT*, **66**, 363

Willman, B., & Strader, J. 2012, *AJ*, **144**, 76

Winteler, C., Käppeli, R., Perego, A., et al. 2012, *ApJL*, **750**, L22

Wood, M. P., Lawler, J. E., Den Hartog, E. A., et al. 2014a, *ApJS*, **214**, 18

Wood, M. P., Lawler, J. E., Sneden, C., et al. 2013, *ApJS*, **208**, 27

Wood, M. P., Lawler, J. E., Sneden, C., et al. 2014b, *ApJS*, **211**, 20